Multiple Shock Fronts in RBS 797: The Chandra Window on Shock Heating in Galaxy Clusters

F. Ubertosi[1,2], M. Gitti[1,3], F. Brighenti[1,4], M. McDonald[5], P. Nulsen[6,7], M. Donahue[8], G. Brunetti[3], S. Randall[9], M. Gaspari[10], S. Ettori[2,11], M. Calzadilla[5], A. Ignesti[12], L. Feretti[3], and E. L. Blanton[13]

[1] Dipartimento di Fisica e Astronomia, Universitá di Bologna, via Gobetti 93/2, I-40129 Bologna, Italy; francesco.ubertosi2@unibo.it
[2] INAF, Osservatorio di Astrofisica e Scienza dello Spazio, via P. Gobetti 93/3, I-40129 Bologna, Italy
[3] Istituto Nazionale di Astrofisica (INAF)—Istituto di Radioastronomia, via Gobetti 101, I-40129 Bologna, Italy
[4] University of California Observatories/Lick Observatory, Department of Astronomy and Astrophysics, Santa Cruz, CA 95064, USA
[5] Kavli Institute for Astrophysics and Space Research, Massachusetts Institute of Technology, Cambridge, MA 02139, USA
[6] Chandra X-ray Center, Smithsonian Astrophysical Observatory, 60 Garden Street, Cambridge, MA 02143, USA
[7] ICRAR, University of Western Australia, 35 Stirling Highway, Crawley, WA 6009, Australia
[8] Department of Physics and Astronomy, Michigan State University, East Lansing, MI 48824, USA
[9] Center for Astrophysics, Harvard & Smithsonian, 60 Garden Street, Cambridge, MA 02138, USA
[10] Department of Astrophysical Sciences, Princeton University, Princeton, NJ 08544, USA
[11] INFN, Sezione di Bologna, viale Berti Pichat 6/2, I-40127 Bologna, Italy
[12] INAF—Astronomical Observatory of Padova, vicolo dell'Osservatorio 5, I-35122 Padova, Italy
[13] Institute for Astrophysical Research and the Department of Astronomy, Boston University, Boston, MA 02215, USA

Abstract

Using $\sim$427 ks of Chandra observations, we present a study of shock heating and intracluster medium (ICM) cooling in the galaxy cluster RBS 797. We discover three nested pairs of weak shocks at roughly 50, 80, and 130 kpc from the center. The total energy associated with the shocks is $\sim$$6 \times 10^{61}$ erg, with the central active galactic nucleus (AGN) driving a pair of weak shocks every 20–30 Myr with a power $P_{sh} \approx 10^{46}$ erg s^{-1}. Based on its morphology and age ($\sim$30 Myr), the inner cocoon shock is associated with the four equidistant X-ray cavities previously discovered. From the thermodynamic analysis of the inner 30 kpc, we find evidence for ICM condensation into colder gas between and behind the X-ray cavities. The total AGN mechanical power (cavities and shocks) of 3.4×10^{46} erg s^{-1} can balance the ICM radiative losses, estimated as $L_{cool} = 2.3 \times 10^{45}$ erg s^{-1}. By building plots of P_{cav} versus L_{cool}, P_{shock} versus L_{cool}, and P_{tot} versus L_{cool} for RBS 797 and 14 other galaxy clusters, galaxy groups, and elliptical galaxies where both cavities and shocks are detected, we verify that the most powerful outbursts are found in the strongest cooling systems. Ultimately, we observe that the mechanical power of the AGN exceeds the gas radiative losses by a factor that is different for FR I and FR II radio galaxies, being less than a few tens for FR Is (as RBS 797) and more than roughly 100 for FR IIs.

Unified Astronomy Thesaurus concepts: Intracluster medium (858); Galaxy clusters (584); Fanaroff-Riley radio galaxies (526); Radio galaxies (1343); Cooling flows (2028); Active galactic nuclei (16)

1. Introduction

In the last two decades, multiwavelength observations and theoretical studies of galaxy clusters, galaxy groups, and elliptical galaxies have revolutionized the understanding of the effects of active galactic nuclei (AGNs) on the surrounding gaseous halos (for reviews, see, e.g., Mathews & Brighenti 2003; Donahue & Voit 2004, 2022; McNamara & Nulsen 2007, 2012; Fabian 2012; Gitti et al. 2012; Gaspari et al. 2020; Eckert et al. 2021). In particular, it has been determined that a feedback loop regulates the interaction between the intracluster medium (ICM) and the central AGN in the brightest cluster galaxy (BCG). According to this scenario, the radiative losses of the ICM lead to the formation of dense central regions of low-temperature gas (the so-called "cool cores"; see, e.g., Hudson et al. 2010) that may constitute large reservoirs of gas to fuel both star formation and the central supermassive black holes (SMBHs). However, in cool cores, the amount of cold material actually observed to be accumulating around BCGs is less than what is expected

from uninterrupted cooling of the X-ray emitting atmosphere (Boehringer et al. 1993; Donahue & Voit 2004; Peterson & Fabian 2006). This discrepancy can be accounted for by considering that AGN activity is triggered in response to the buildup of these reservoirs and is able to regulate the thermodynamic state of the gas (e.g., McNamara & Nulsen 2007, 2012; McNamara et al. 2016; McDonald et al. 2018; Donahue & Voit 2022).

On the one hand, the relativistic AGN jets have a tremendous impact on the gas morphology and thermodynamics, carving large holes (the X-ray cavities) and driving shocks in the ICM, which have been observed in the X-ray band (e.g., Churazov et al. 2000; Wise et al. 2007; Gitti et al. 2011; Vantyghem et al. 2014; Randall et al. 2015; Snios et al. 2018). These outbursts typically inject between 10^{56} and 10^{62} erg into the environment, with the more energetic events being found, on average, in the largest cool cores (Bîrzan et al. 2004; Rafferty et al. 2006; McDonald et al. 2018). Such an outcome of AGN feedback may explain how further cooling of the ICM can be limited.

On the other hand, AGN activity can also stimulate cooling of the ICM. The mechanical thrust imparted to the gas by the rising X-ray cavities can uplift the central cool material to

several tens of kiloparsecs, where cooling times and dynamical times become comparable (e.g., Revaz et al. 2008; Brighenti et al. 2015; McNamara et al. 2016). Alternatively, the turbulence injected by the nuclear activity may trigger local compressions of the gas (e.g., Brighenti & Mathews 2002; Gaspari et al. 2011, 2012). In such cases, as thermal instabilities may ensue, further cooling of the ICM can be stimulated, creating warm or cold filaments (e.g., McDonald et al. 2010; Russell et al. 2019; Calzadilla et al. 2022; Temi et al. 2022; Olivares et al. 2022).

Regarding the observational footprints of feedback, AGN-inflated cavities are the most evident outcomes of radio lobe expansion in the ICM and have been observed in numerous galaxy clusters, galaxy groups, and elliptical galaxies (e.g., Bîrzan et al. 2004; Rafferty et al. 2006; Shin et al. 2016). Since the enthalpy of the bubbles is a proxy for the energy deposited by the jet, the study of large samples of radio galaxies in clusters has provided constraints on the relation between the synchrotron radio power and the kinetic power (e.g., Bîrzan et al. 2004, 2008, 2012; Cavagnolo et al. 2010; O'Sullivan et al. 2011). Specifically, from these relations, it has been determined that for both high (Fanaroff–Riley type IIs, FR IIs) and low (Fanaroff–Riley type Is, FR Is; Fanaroff & Riley 1974) radio luminosity radio galaxies, the total radio power roughly scales with the mechanical luminosity, which is usually larger by a factor of 100 (see also Gitti et al. 2012; Fujita et al. 2016), implying that the mechanical feedback response largely exceeds the radiative one. Thus, the investigation of the hot gas surrounding radio galaxies in clusters and groups can be undertaken to probe feedback, SMBH jet formation, and AGN mechanical power.

In a fraction of clusters, groups, and elliptical galaxies, multiple X-ray cavities at different distances from the center have been detected, indicating successive episodes of radio activity in the BCG (e.g., Dunn et al. 2005; Fabian et al. 2005; Wise et al. 2007; Vantyghem et al. 2014; Hlavacek-Larrondo et al. 2015; Randall et al. 2015). Such discoveries made it possible both to probe the AGN response to ICM cooling over time and to recover valuable information on the duty cycle of AGNs. In particular, it has been determined that, on average, every few tens of megayears, the central AGN initiates a new cycle of activity, inflating new lobes and excavating additional pairs of cavities (e.g., Bîrzan et al. 2004, 2012; Babul et al. 2013; Vantyghem et al. 2014; Randall et al. 2015; Biava et al. 2021). While several aspects related to X-ray cavities are yet to be fully understood (see, e.g., Eckert et al. 2021; Donahue & Voit 2022), their general role in heating the environment has been extensively investigated and verified.

More uncertain is the role of shock heating in galaxy clusters. Simulations of jet expansion in the ICM indicate that besides excavating the bubbles, the gas-piercing jet also drives weak shocks (with Mach numbers between 1.1 and 1.3) that typically assume the shape of cocoons surrounding the X-ray cavities (e.g., Heinz & Churazov 2005; Brighenti & Mathews 2006; Brüggen et al. 2007; Cielo et al. 2018; Martizzi et al. 2019; Wittor & Gaspari 2020). The energy injected in shocks is not only deposited along the jet axis (or ahead of the X-ray cavities) but distributed over the whole azimuth (e.g., Brighenti & Mathews 2006; Mathews et al. 2006; Martizzi et al. 2019; Huško et al. 2022). Besides the power required to inflate X-ray cavities, also considering the mechanical power of weak shocks provides an opportunity to truly test the efficiency

of AGNs in effectively keeping the ambient gas from rapid cooling (e.g., McNamara & Nulsen 2012; Randall et al. 2015; Eckert et al. 2021). However, direct observational evidence of weak shocks in galaxy clusters is rare. Weak shocks driven by central AGNs have been discovered in roughly a dozen systems (Liu et al. 2019), all targeted with deep Chandra exposures, which is lower than the number of known X-ray cavities by more than an order of magnitude (e.g., Shin et al. 2016). Given the paucity of detected shocks, little is known about their role in the feedback cycle. By analyzing a collection of 13 objects with detected shocks and X-ray cavities, Liu et al. (2019) found that the AGN mechanical energy is roughly equally divided between shocks and X-ray cavities. Nevertheless, it would also be interesting to dissect the role of shock heating and energy partition with cavities over time, which would allow the stability of the jet kinetic power across succeeding episodes of AGN activity to be addressed more robustly. So far, the unique case of the galaxy group NGC 5813 (Randall et al. 2011, 2015), where three groups of concentric and aligned shock fronts, each associated with expanding X-ray cavities, has demonstrated that the average jet mechanical power can be stable over roughly 50 Myr. Additionally, Randall et al. (2015) found that shocks alone can compensate for the radiative losses of the ICM, indicating that shock heating may be a relatively important contribution to the AGN/ICM feedback cycle. While these results indicate that the intragroup medium of galaxy groups is strongly affected by AGN feedback, these systems also have shallower gravitational potentials compared to galaxy clusters (e.g., Giodini et al. 2010; McCarthy et al. 2010); thus, the effect of AGN-launched shocks on the gas may be more pronounced. As such, the conclusions based on observations of groups may not be applicable to galaxy clusters. The detection of multiple shock fronts driven by AGN activity in a galaxy cluster would expand the number of objects with known weak shocks but, more importantly, would allow us to address the question of how much heating by weak shocks contributes to the feedback cycle in clusters of galaxies.

1.1. The Galaxy Cluster RBS 797

An interesting cool core galaxy cluster to investigate these topics is RBS 797 ($z = 0.354$), located at R.A. 09:47:12.76, decl. +76:23:13.74. The cluster hosts an FR I radio galaxy at its center, showing multiple radio lobe pairs that are misaligned by roughly 90° (see Gitti et al. 2006; Cavagnolo et al. 2011; Gitti et al. 2013), with the largest and brightest lobes extended in the east (E)–west (W) direction, smaller lobes in the north (N)–south (S) direction, and perpendicular jet pairs in the inner ~10 kpc. Gitti et al. (2013) proposed that the multifaceted morphology of the radio galaxy is caused either by rapid reorientation of the AGN jets between different cycles of central radio activity or by the presence of twin active SMBHs in the core of the BCG. Early Chandra observations revealed that deep E–W X-ray cavities are associated with the E–W radio lobes (Schindler et al. 2001; Gitti et al. 2006; Doria et al. 2012) and that the large mechanical power of the bubbles (Cavagnolo et al. 2011 estimated ≈3–6 × 10^{45} erg s^{-1}) is of the order of the radiative losses in the ICM, indicating that feedback may be efficient in this galaxy cluster. Moreover, Cavagnolo et al. (2011) noted the presence of two surface brightness edges in the ICM. The first one surrounds the E–W X-ray cavities at ~50 kpc from the center and has been

proposed to be a combination of cool gas rims encasing the X-ray cavities and a cocoon shock surrounding the bubbles. However, due to the insufficient number of counts collected by the old Chandra exposures, no detailed morphological or spectral study of this putative shock has been performed. The second edge was tentatively identified at ∼80 kpc from the center, but again, no classification was possible. Overall, the above findings point to RBS 797 being an interesting target to study the history of AGN activity in galaxy clusters and the effect of shock heating on the ICM throughout the successive central radio activities.

Recently, we presented the first results from the analysis of the deeper Chandra observations (Cycle 21 LP proposal, 420 ks, PI: Gitti; plus the previous ∼50 ks observations), focused on the cavity system only (Ubertosi et al. 2021). We found that the N–S radio lobes also have inflated X-ray cavities at the same projected distances as the deep E–W ones. The geometry of the inner ∼50 kpc of RBS 797 is thus peculiar, showing equidistant, centrally symmetric, and perpendicular X-ray cavities. By measuring the age of the X-ray cavities, we found that the two outbursts are nearly coeval, with a time difference of ≲10 Myr, which is consistent with both scenarios of a rapid reorientation (see also Soker 2022) and a coeval activity of binary AGNs.

In this paper, we present the full analysis of the old and new Chandra observations of RBS 797, focusing on characterizing the whole cool core region and investigating AGN feedback by both shocks and cavities. This paper is organized as follows. Section 2 describes the observations used in this work. Section 3 presents the search and characterization of weak shocks propagating in the ICM. Section 4 presents the X-ray analysis of the cluster, with specific subsections focused on the investigation of radial spectral profiles (Section 4.1), maps of thermodynamic quantities (Section 4.2), and the ICM abundance distribution (Section 4.3). In Section 5, we determine the spectral properties of the central X-ray point source. In Section 6, we discuss our results, considering the implications of our findings on the history of AGN activity (Section 6.1), the heating and cooling balance (Section 6.2), and the role of shock heating in galaxy clusters, groups, and elliptical galaxies (Section 6.3). Finally, we summarize our conclusions in Section 7.

We assume a ΛCDM cosmology with $H_0 = 70$ km s^{-1} Mpc^{-1}, $\Omega_{\rm m} = 0.3$, and $\Omega_\Lambda = 0.7$, which gives a scale of 4.9 kpc arcsec^{-1} at $z = 0.354$. Uncertainties are reported at 1σ, unless otherwise stated. Position angles (P.A.) of ellipses are defined northward from W along the major axis. The radio spectral index α is defined as $S_\nu \propto \nu^{-\alpha}$.

2. The Data

2.1. X-Ray: Chandra

The data have been reprocessed using CIAO-4.13 and CALDB-4.9.6. The 15 available ObsIDs (summarized in Table A1) sum up for a total, uncleaned exposure time of 458 ks. In our region of interest (within ∼500 kpc from the center), the available 0.5–7 keV total exposure contains ∼300,000 net counts, which allow for a thorough analysis of the cool core region. The removal of background flares reduced the total exposure by ∼9% to roughly 427 ks. To correct the astrometry of the 15 ObsIDs, the longest observation (ObsID 22932) was shifted (using the wcs_match tool) so that the

coordinates of the central X-ray point source match those of the AGN from high-resolution radio observations (R.A.: 09 47 12.76, decl.: +76 23 13.74; Gitti et al. 2013). Then, the other ObsIDs were reprojected to match the longest one. Background files were obtained from blank sky event files, normalized to the 9–12 keV count rate of the observations. More details on the Chandra data reduction procedures can be found in Ubertosi et al. (2021).

We produced a merged, exposure-corrected, background-subtracted Chandra image in the 0.5–7 keV band with the merge_obs script that reprojects and combines multiple ObsIDs. The resulting image is shown in Figure 1. Notable features in the image have been investigated using CIAO and Proffit, while spectral fitting (in the 0.5–7 keV band, with a binning of 25 counts bin^{-1}) has been performed using Xspec12.10, selecting the table of solar abundances of Asplund et al. (2009). An absorption model (tbabs) was always included to account for Galactic absorption, with the column density fixed at $N_{\rm H} = 2.28 \times 10^{20}$ cm^{-2} (HI4PI Collaboration et al. 2016). For models with redshift as a parameter, we froze it to the value of the cluster ($z = 0.354$).

When analyzing the thermodynamic properties of the ICM, the spectra extracted from the 15 ObsIDs were jointly fitted with a combination of different models.

1. The model tbabs*apec is composed of a photoelectric absorption model (tbabs) convolved with a thermal model (apec). The column density and redshift were fixed, while the other parameters (temperature kT, abundance, and normalization) were left free to vary.

2. The model projct*tbabs*apec combines the previous model with the component projct, which computes the combined spectra of emission from a set of nested shells projected into annular regions. The inclusion of this component allows us to derive the deprojected electron density $n_{\rm e}$ of the ICM by combining the normalization (norm) of the apec component with the volume (V) of the emitting region. Assuming $n_{\rm e} = 1.2 n_{\rm H}$, $n = n_{\rm e} + n_{\rm H} = 1.83 n_{\rm e}$ (where n and $n_{\rm H}$ are the total density and proton density, respectively), the electron density can be estimated as

$$n_{\rm e} = \sqrt{10^{14}\left(\frac{4\pi \times {\rm norm} \times [D_{\rm A}(1+z)]^2}{V/1.2}\right)}, \quad (1)$$
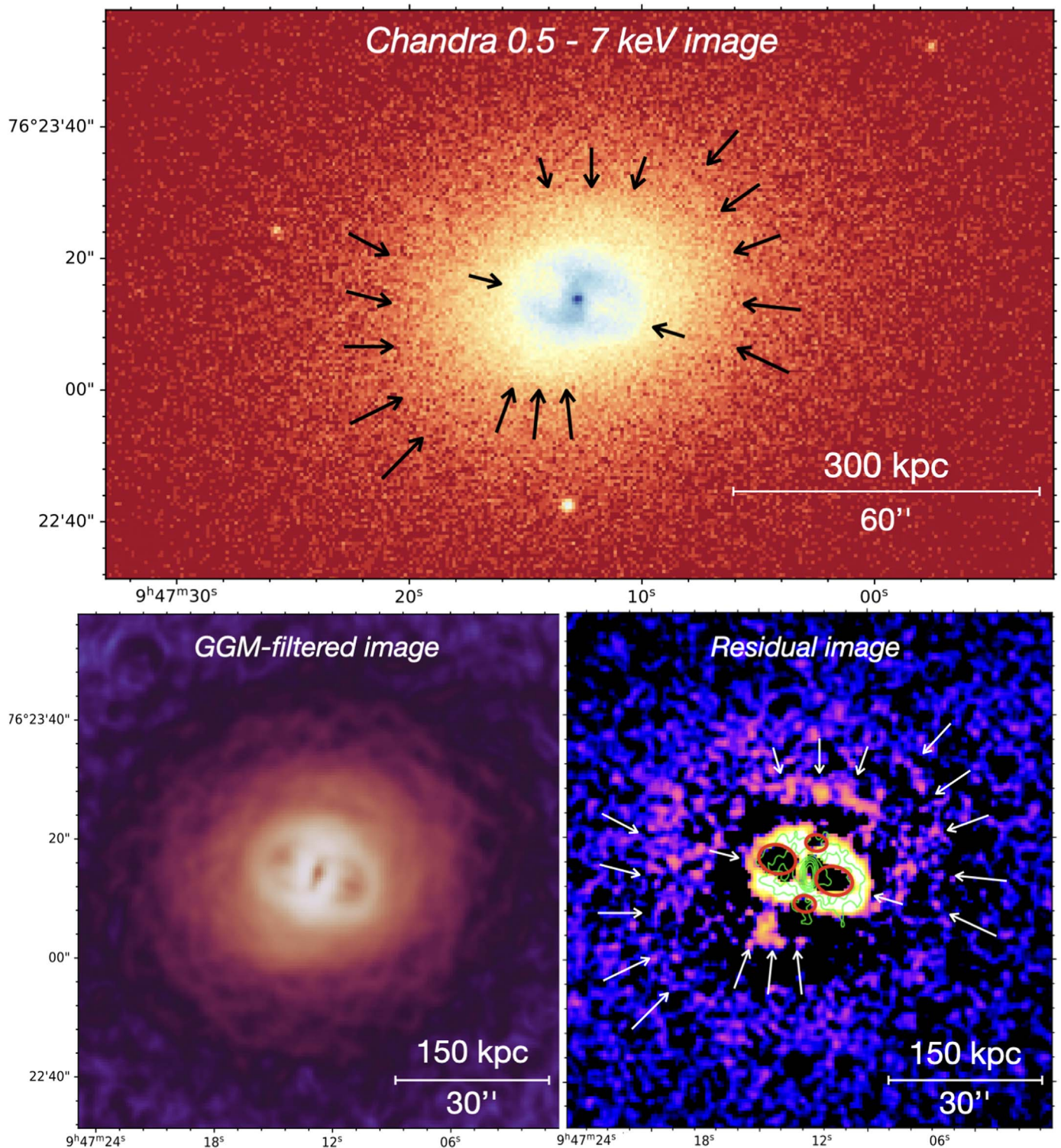
where $D_{\rm A}$ is the angular diameter distance (1026 Mpc for RBS 797). The electron density can then be combined with the deprojected temperature of the apec component to obtain the pressure p, entropy S, and cooling time $t_{\rm cool}$ of the ICM, defined as

$$p = nkT, \quad (2)$$

$$S = \frac{kT}{n_{\rm e}^{2/3}}, \quad (3)$$

$$t_{\rm cool} = \frac{\gamma}{\gamma - 1} \frac{kT}{\mu \, X \, n_{\rm e} \, \Lambda(T)}, \quad (4)$$

where $\gamma = 5/3$ is the adiabatic index, $\mu \approx 0.6$ is the mean molecular weight, $X \approx 0.7$ is the hydrogen mass fraction, and $\Lambda(T)$ is the cooling function (Sutherland & Dopita 1993).

Figure 1. Top panel: background-subtracted, exposure-corrected Chandra image of RBS 797 in the 0.5–7 keV band. Bottom left panel: Chandra image filtered with the GGM method using $\sigma = 2''$. Bottom right panel: double β-model residual image of RBS 797, highlighting the four X-ray cavities (red ellipses). The green contours at 1.4 GHz (at 3, 5, 10, 20, 40, 75, and $150\times$ the rms of 0.02 mJy beam^{-1}, at $\sim 1''5$ resolution; see Gitti et al. 2006) show the morphology of the central radio galaxy. In the top and bottom right panels, the arrows indicate the position of the surface brightness edges at progressively increasing distances from the center. See Section 3 for details.

2.2. Radio: VLA

To allow a comparison with the X-ray data, we employ the archival radio observations of RBS 797 performed with the Very Large Array (VLA) at 1.4 GHz originally presented by Gitti et al. (2006) and Doria et al. (2012). In particular, we show the radio contours generated from the array A observation (rms = 0.02 mJy beam^{-1}, $\sim 1''5$ resolution; see Figure 2(b) in Gitti et al. 2006) that best emphasize the structure of the radio galaxy and its interaction with the ICM in the inner ~ 50 kpc of the cluster. Additionally, to investigate the radio/X-ray

interaction at larger scales (~100 kpc), we show the radio contours obtained from the combined A-B-C array observations (rms = 0.01 mJy beam^{-1}, ~3″ resolution; see Doria et al. 2012). We also show in Section 6.1 the preliminary contours of our new Jansky Very Large Array (JVLA) observations at 3 GHz, whose detailed analysis is still under way and will be presented in a forthcoming paper (F. Ubertosi et al. 2023, in preparation).

3. Shock Fronts in the ICM

The top panel of Figure 1 shows the background-subtracted, exposure-corrected Chandra image. In the bottom panels, we show the original image filtered with the Gaussian gradient magnitude (GGM) filter (Sanders et al. 2016) with a 2″ filter and the residual Chandra image (originally presented in Ubertosi et al. 2021, obtained by subtracting a 2D double β-model from the Chandra image). In the inner ~50 kpc, there are the four equidistant X-ray cavities already discussed in Ubertosi et al. (2021), best visible in the residual image (right panel). Beyond the X-ray cavities, the images reveal the presence of three distinct and nested surface brightness edges at approximate projected distances from the center of ~50, ~80, and ~130 kpc. In the following, we refer to the three features as inner, middle, and outer edges.

The inner edge surrounds the AGN-inflated cavities and consists of an ellipse with P.A. ≈ 345° and ellipticity (ratio between major and minor axes) of ~1.2. The edge is located at a distance along the major axis of ~11″ (54 kpc) and appears stronger along the E–W direction. Within this shell of bright X-ray emission, there are the four cavities (at a distance of ~5″.5 from the center; see Ubertosi et al. 2021) and the surrounding rims (at a distance of ~8″ from the center). The middle edge appears sharper in the N–S direction and is described by an ellipse with P.A. ~ 20° and ellipticity 1.1. The outer edge is described by an ellipse with P.A. ~ 100° and ellipticity 1.1 and is particularly pronounced in the E–W direction. While the inner and middle edges were already noted by Cavagnolo et al. (2011), the deeper Chandra observations allowed us to recover the third outer edge. Most importantly, thanks to the higher number of counts, we are able to perform a thorough morphological and spectral analysis of such edges for the first time (see Section 3.1).

3.1. Detailed Properties of the Shocks

Our aim is to secure the identification and further investigate the properties of the edges visible in Figure 1. In particular, this requires one to (i) identify the exact position and magnitude of each front by studying the surface brightness profile across the edge and (ii) measure the thermodynamic properties (e.g., temperature and pressure) inside and outside the front to determine its nature. In the following, we first describe the procedure we employed to search for and investigate shock fronts, and then we present the results for RBS 797.

We performed a systematic search for edges in the ICM by extracting surface brightness profiles (centered on the X-ray centroid that coincides with the AGN in the BCG) in circular or elliptical sectors of varying opening angles (between 30° and 90°) and different binning (between 0″.7 and 2″). This strategy was adopted to determine the geometry that best describes the fronts. The resulting profiles were visually inspected to identify

possible jumps in surface brightness. For each edge, the profile was fit in Proffit with a single power-law model and a broken power-law model; a surface brightness edge at distance r_J and characterized by a density jump J was considered a detection if an F-test between the single and the broken power law indicated a significant statistical improvement (more than 99% confidence). For the detected surface brightness edge, the Mach number $\mathcal{M}$ of the front was derived from the best-fit density jump J using the Rankine–Hugoniot conditions (see, e.g., Markevitch & Vikhlinin 2007):

$$\mathcal{M} = \left(\frac{3J}{4-J}\right)^{1/2}. \tag{5}$$

Moreover, the Mach number can be used to predict the expected temperature and pressure jumps, again using the Rankine–Hugoniot conditions:
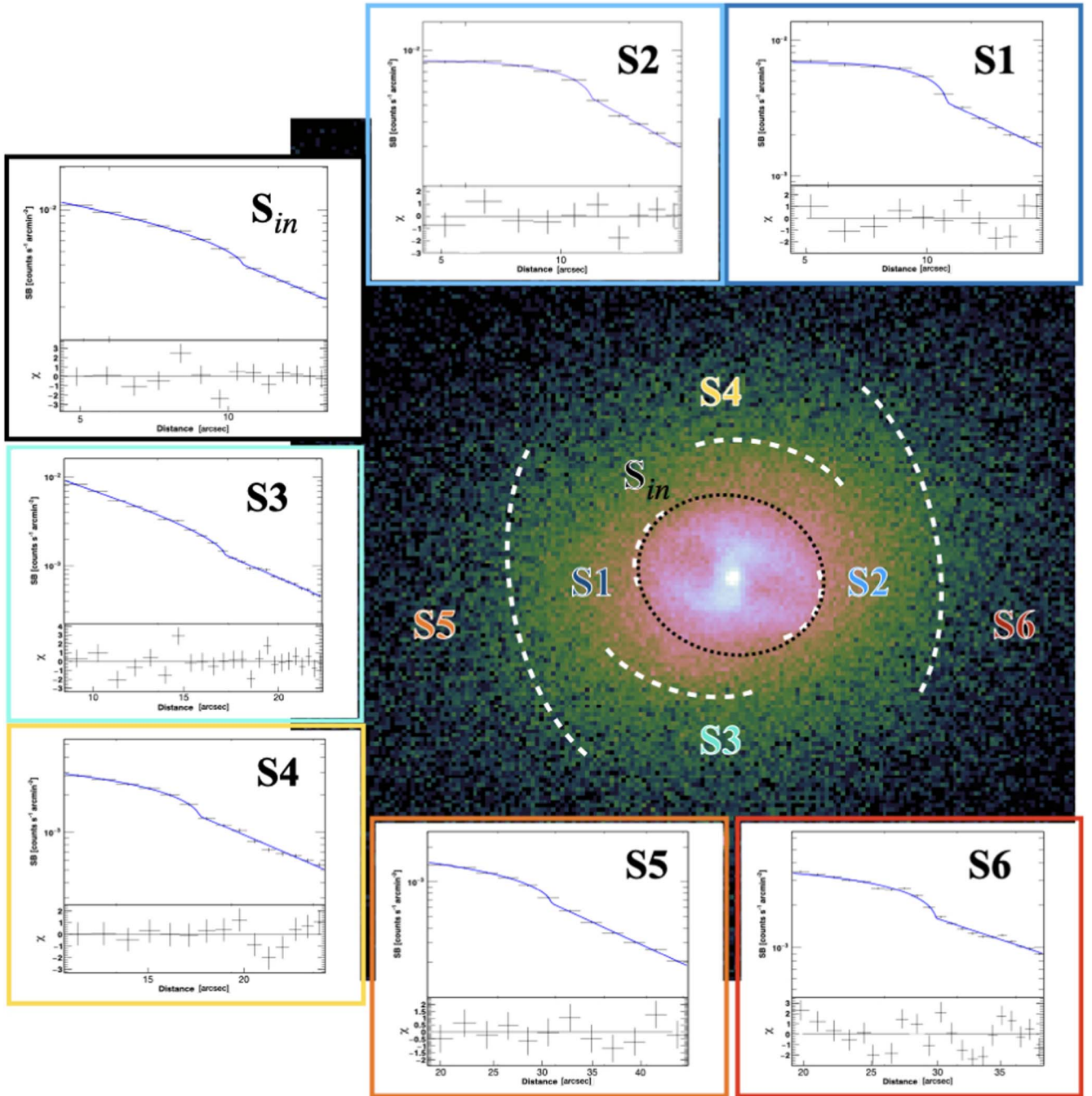
$$T_{\text{jump}}^{\text{exp}} = \frac{5\mathcal{M}^4 + 14\mathcal{M}^2 - 3}{16\mathcal{M}^2}, \tag{6}$$

$$p_{\text{jump}}^{\text{exp}} = \frac{5\mathcal{M}^2 - 1}{4}. \tag{7}$$

To measure the spectral properties of the detected surface brightness jumps, we extracted the spectra of three concentric regions. The first region is a wedge extending between $0.75r_J$ and r_J, the second is a wedge extending between r_J and $1.5r_J$, and the third wedge extends from $1.5r_J$ to the edge of the Chandra image and allows for deprojection. These bin widths were chosen to avoid the inclusion of thermal emission far from the jump; while selecting larger regions would increase the number of counts, it may also lead to smearing thermodynamic gradients. Spectra were fitted with a projct*tbabs*apec model to measure the deprojected temperature and density (Equation (1)), which were combined to derive the pressure jump across each edge (Equation (2)).

Applying the above procedure to RBS 797 allowed us to confirm the shock front nature of the three concentric and nested systems of edges noted in the previous paragraphs. In Figure 2, we show the arc region that best describes each front and the fitted surface brightness profiles, while in Table B1 of Appendix B and Table 1, we report the surface brightness analysis and thermodynamic properties of the shocks, respectively. The details of the spectral fitting are shown in Table B2 and Figure B1 of Appendix B, while below, we report the main properties of each detected shock.

Inner edges (S1, S2, S$_{\text{in}}$)—The innermost surface brightness edge in RBS 797 is the bright cocoon surrounding the four X-ray cavities. By extracting the surface brightness profile in elliptical sectors (with ellipticity 1.2 and P.A. 345°), we recovered sharp and significant density jumps between angles 130°–190° and 310°–15°, i.e., beyond the E–W cavities (first two rows in Table B1; S1 and S2 panels in Figure 2). The edges are located at roughly 10″–11″ (≈50–55 kpc) from the center. We name these inner east and west edges S1 and S2, respectively. By substituting the fitted density jumps in Equation (5), we measured Mach numbers $\mathcal{M}_{\text{S1}} = 1.33 \pm 0.05$ and $\mathcal{M}_{\text{S2}} = 1.27 \pm 0.04$. The spectral analysis confirms the shock front nature of the edges (first two rows of Table 1); S1 is characterized by a temperature jump $T_{\text{jump}}^{\text{obs}} = 1.35 \pm 0.18$ and a pressure jump $p_{\text{jump}}^{\text{obs}} = 1.80 \pm 0.24$. The front S2 is less pronounced, being associated with a temperature jump of $T_{\text{jump}}^{\text{obs}} = 1.13 \pm 0.08$ and

Figure 2. Central panel: 0.5–7 keV Chandra image of RBS 797. The white (black) dashed regions indicate the positions and extents of the arc-like (cocoon-like) edges found on opposite sides of the center, as results from the surface brightness analysis reported in Table B1. Colored labels indicate the name of each edge. Subpanels: surface brightness profile across each edge fit with the broken power-law model (blue line) described in Table B1. Residuals of the fit are shown in the bottom box of each plot.

$p_{jump}^{obs} = 1.50 \pm 0.13$. While the lower Mach number of S2 compared to S1 is consistent with a less pronounced shock to the W, it is also possible that this is due to projection effects; low-temperature gas in the W cavity rims, projected in front of the S2 front, may be damping the temperature gradient (similar to what has been found for Hydra A; see Gitti et al. 2011).

As the geometry of the edge is suggestive of a cocoon shock propagating in the ICM, we also analyzed the radial profile extracted from a complete ellipse with ellipticity 1.2 and P.A. 345°. We found a density jump (named S_{in}) at $\sim10\rlap{.}''7$ (52.4 kpc) from the center with a Mach number $\mathcal{M}_{S_{in}} = 1.20 \pm 0.03$. With the spectral analysis, we found a

temperature jump of $T_{jump}^{obs} = 1.18 \pm 0.07$ and a pressure jump of $p_{jump}^{obs} = 1.88 \pm 0.16$ (see Figure 2 and third row of Tables B1 and 1). Thus, the inner edge is continuous around the azimuth and consists of a cocoon shock driven by the jets of the central AGN. The lower Mach number of S_{in} with respect to S1 and S2 probably indicates that the shock strength varies with azimuth (as also found in, e.g., Hydra A; Gitti et al. 2011), so $\mathcal{M}_{S_{in}}$ is the result of an average across the azimuth. Thus, we suggest that S1 and S2 are the highest Mach number parts of a single shock (S_{in}). In this respect, the ellipticity of S_{in} (1.2) provides an indication of the ratio of the mean shock speeds along the major and minor axes.

Table 1
Properties of the Nested Shocks in RBS 797

Shock	r_{sh} (kpc (arcsec))	$\mathcal{M}$	T_{jump}^{exp}	p_{jump}^{exp}	T_{jump}^{obs}	p_{jump}^{obs}	t_{age} (Myr)	E_{sh} (10^{60} erg)	P_{sh} (10^{45} erg s^{-1})
(1)	(2)	(3)	(4)	(5)	(6)	(7)	(8)	(9)	(10)
S1–inner east	53.9 (11.0)	1.33 ± 0.05	1.33 ± 0.05	1.98 ± 0.17	1.35 ± 0.18	1.80 ± 0.24	28.5 ± 2.4	8.3 ± 1.7	8.6 ± 1.8
S2–inner west	50.5 (10.3)	1.27 ± 0.04	1.26 ± 0.04	1.77 ± 0.08	1.13 ± 0.08	1.50 ± 0.13	32.8 ± 2.8	4.2 ± 0.8	4.1 ± 0.8
S_{in}–inner total	52.4 (10.7)	1.20 ± 0.03	1.19 ± 0.02	1.54 ± 0.06	1.18 ± 0.07	1.88 ± 0.16	33.4 ± 1.3	6.6 ± 0.5	6.3 ± 0.6
S3–middle south	79.4 (16.2)	1.20 ± 0.03	1.19 ± 0.03	1.54 ± 0.08	1.23 ± 0.11	1.67 ± 0.21	50.9 ± 4.3	8.0 ± 1.9	5.0 ± 1.2
S4–middle north	81.8 (16.7)	1.19 ± 0.03	1.18 ± 0.03	1.51 ± 0.10	1.24 ± 0.12	2.36 ± 0.29	54.9 ± 4.5	6.3 ± 1.5	3.7 ± 0.8
S5–outer east	136 (27.7)	1.19 ± 0.03	1.18 ± 0.03	1.49 ± 0.08	1.37 ± 0.26	1.91 ± 0.41	84.7 ± 6.4	18.5 ± 5.5	7.0 ± 2.1
S6–outer west	129 (26.3)	1.25 ± 0.04	1.24 ± 0.03	1.70 ± 0.10	1.41 ± 0.24	2.34 ± 0.43	82.8 ± 6.9	19.9 ± 3.0	7.7 ± 1.5

Note. (1) Shock label; (2) distance of the shock from the center (measured from the front mid-aperture); (3) Mach number of the shock, obtained from the density jump reported in Table B1; (4) and (5) temperature and pressure jumps predicted by the Mach number; (6) and (7) observed temperature (deprojected) and pressure jumps, obtained from the fit to the spectrum of the ICM in the downstream and upstream sides of the edge (see Table B2); (8) age of the shock (see Equation (8)); (9) energy of the shock (see Equation (10)); (10) shock power, defined as $P_{sh} = E_{sh}/t_{age}$. The energy and power of fronts S1, S2, S3, S4, S5, and S6 are referred to the half ellipsoid covered by each front, while for S_{in}, the full ellipsoid was considered (see text for details).

Middle edges (S3 and S4)—The second front identified from the images in Figure 1 is located at a distance of 16″–17″ (≈80 kpc) from the center. Extracting surface brightness profiles from elliptical sectors (ellipticity 1.1 and P.A. 20°) revealed two significant jumps S (S3; angles 200°–270°, Mach number $\mathcal{M}_{S3} = 1.24 \pm 0.03$) and N (S4; angles 45°–110°, Mach number $\mathcal{M}_{S4} = 1.30 \pm 0.08$) of the center. The spectral analysis revealed that the shock front S3 has a temperature jump $T_{jump}^{obs} = 1.23 \pm 0.11$ and a pressure jump $p_{jump}^{obs} = 1.67 \pm 0.21$, while the shock front S4 has a temperature jump $T_{jump}^{obs} = 1.24 \pm 0.12$ and a pressure jump $p_{jump}^{obs} = 2.36 \pm 0.29$ (see Figure 2 and Tables B1 and 1). We tested whether S3 and S4 may be part of a single front over 360°, as done for the inner edge, but the surface brightness profile from the complete ellipse did not reveal any significant jump.

Outer edges (S5 and S6)—The presence of a third set of fronts at a distance of ≈27″ (or 135 kpc) from the center was not noticed in previous studies of RBS 797. Outer edges in surface brightness to the E–W are visible in the images of Figure 1. Fitting surface brightness profiles to the E–W in elliptical sectors (ellipticity 1.1 and P.A. 102°) returned evidence for prominent density jumps at the location of the edges (between angles 140°–252° and 304°–87°; see Figure 2 and last two rows of Tables B1 and 1). In particular, we find that the eastern outer front (S5) has a Mach number $\mathcal{M}_{S5} = 1.19 \pm 0.03$ and coincides with jumps in temperature and pressure of 1.37 ± 0.26 and 1.91 ± 0.41, respectively. The western outer front is traveling with a Mach number $\mathcal{M}_{S6} = 1.25 \pm 0.04$ and coincides with jumps in temperature and pressure of 1.41 ± 0.24 and 2.34 ± 0.43, respectively.

Overall, the above results confirm the existence of three groups of nested shock fronts in the ICM of RBS 797. The significance of the measured density jumps J is more than ~6σ (see Table B1). For the inner and middle edges, the significance of the measured temperature jumps is between 2σ and 3σ, while the significance of the pressure jumps is between 3σ and 5σ. For the outer edge, the significance of the temperature and pressure jumps is between 1.5σ and 3σ. Moreover, the predicted and measured temperature and pressure jumps are in agreement within the errors (see Table 1, columns (4)–(7)). With Mach numbers in the range 1.2–1.3, the edges can be classified as weak shocks, likely resulting from successive

energy injection events by the AGN activity. It is interesting to note the continual change in P.A. of the different shock groups: from E–W (inner shocks) to N–S (middle shocks) and again to E–W (outer shocks). It is likely that the middle and outer opposed shock arcs represent the highest Mach number parts of complete middle and outer cocoon shocks that encompass the whole azimuth, respectively, as we were able to verify for the inner jump. For instance, we might not be able to detect middle E–W surface brightness jumps, as these would be located in a rather narrow region in between the inner and outer E–W fronts, which would prevent the surface brightness profile at the interface of the shocks from being accurately measured. Besides, it is known that the central AGN in RBS 797 is characterized by multiple changes in the P. A. of its lobes and jets (Gitti et al. 2006, 2013; Cavagnolo et al. 2011; Ubertosi et al. 2021), up to 90° misalignment. Thus, the nested groups of opposed and misaligned shock fronts might trace older episodes of differently oriented AGN activity cycles. We further investigate this scenario in Section 6.

3.2. Shock Energetics and Timescales

Measuring the age and energetics of the shocks provides essential information for probing the impact of these features on the cluster thermodynamic conditions. The age of the shocks t_{age} can been determined by assuming that the shock has traveled from the center to its current position (r_{sh}, the distance to the mid-aperture of the front, reported in Table 1) with its observed Mach number $\mathcal{M}$, i.e.,

$$t_{age} = \frac{r_{sh}}{\mathcal{M} \, c_S}, \tag{8}$$

where $c_S = \sqrt{\gamma kT/(\mu m_p)} \approx 5.2 \times 10^2 \sqrt{kT \, [\text{keV}]}$ km s^{-1} is the upstream sound speed (measured from the temperature outside the shock). We note that this method may slightly overestimate the true shock age (by a relatively modest factor of ~10%–20%; see Randall et al. 2011), given that when the shock was initially launched, it likely had a higher Mach number. Using Equation (8), we found an age of 33.4 ± 1.3 Myr for the inner shock S_{in}, 52.9 ± 2.8 Myr for the middle shock (estimated as the average between S3 and

S4), and 83.8 ± 1.4 Myr for the outer shock (average between S5 and S6). See Table 1 for details.

To compute the energy deposited by each shock, we considered the volume of shocked gas and the difference in energy density at the interface (e.g., David et al. 2001; Randall et al. 2015):

$$E_{sh} = \frac{3}{2} V \times \Delta p = \frac{3}{2} V \times (p_{in} - p_{out}). \qquad (9)$$

The above equation can be rewritten in terms of preshock (upstream) pressure p_{out}, shock volume V, and Mach number $\mathcal{M}$ as:

$$E_{sh} = \frac{3}{2} p_{out} \times V \times \left(\frac{5\mathcal{M}^2 - 5}{4} \right). \qquad (10)$$

The pressure inside (downstream) and outside (upstream) each front is known from the spectral analysis of the shocks (see Table B2 in Appendix B). For each front of each shock pair (S1 and S2, S3 and S4, S5 and S6), we computed the volume as that of half of a prolate ellipsoid (assuming that the two fronts of each pair are parts of a single cocoon) of major and minor axes set by the annular sector used for the surface brightness and spectral analysis (see Table B2; for comparison, see also Randall et al. 2011; Snios et al. 2018). For the cocoon front S_{in}, we considered the full prolate ellipsoid. The shock energies are reported in Table 1. For the inner edge, we have two estimates of the total shock energy, i.e., $E_{S1} + E_{S2} = 12.5 \pm 2.5 \times 10^{60}$ erg or $E_{S_{in}} = 6.6 \pm 0.3 \times 10^{60}$. The first method likely represents an upper limit to the true shock energy, as it assumes that the whole shock front has the Mach number of its strongest parts. Thus, we consider $E_{S_{in}}$ as our best estimate for the shock energy. For the middle and outer shocks, we compute the total energy as $E_{sh}^{m} = E_{S3} + E_{S4}$ and $E_{sh}^{o} = E_{S5} + E_{S6}$, respectively, which may overestimate the true shock energy by a factor up to 2 (based on the comparison with the inner edge).

We thus find that the energy rises from the inner shock ($E_{sh}^{in} \sim 0.7 \times 10^{61}$ erg), to the middle shock ($E_{sh}^{m} \sim 1.4 \times 10^{61}$ erg), to the outer shock ($E_{sh}^{o} \sim 3.8 \times 10^{61}$ erg), mostly due to the larger volume occupied by the progressively more distant fronts (see also Randall et al. 2015). These values can be summed up to obtain the total energy injected through shocks in the ICM of RBS 797, that is, $E_{sh}^{tot} = 5.9 \pm 1.5 \times 10^{61}$ erg.

Ultimately, we computed the shock power as the ratio between the shock energy and the shock age, $P_{sh} = E_{sh}/t_{sh}$. This information is crucial to understand how effective the energy injection by shocks is with respect to other forms of energy inputs (e.g., X-ray cavities) or losses (i.e., radiative cooling), a topic we discuss in Section 6. On the one hand, the shock energy computed using Equation (10) may be overestimated by up to a factor of ~ 2 (see Randall et al. 2011). On the other hand, as stated above, the shock ages may also be slightly overestimated. Thus, in computing the shock power as E_{sh}/t_{sh}, these two effects partially compensate for one another. We report the shock powers in Table 1; we estimate total powers of $P_{sh}^{in} = 6.3 \pm 0.6 \times 10^{45}$, $P_{sh}^{m} = 8.7 \pm 1.9 \times 10^{45}$, and $P_{sh}^{o} = 1.5 \pm 0.4 \times 10^{46}$ erg s^{-1}. Since the middle and outer shock powers are based on the highest Mach number parts of the shocks, the true P_{sh}^{m} and P_{sh}^{o} may be slightly lower. It is then possible to conclude that, within the errors, the shock

power has remained nearly constant, releasing roughly $(0.6–1.5) \times 10^{46}$ erg s^{-1} in the ICM for every outburst.

4. Global Properties of the ICM

The following subsections are dedicated to the analysis of the global properties of the ICM in RBS 797. After deriving the radial profiles (Section 4.1) and maps (Section 4.2) of the thermodynamic quantities, we study the abundance distribution in the ICM (Section 4.3).

4.1. Radial Profiles of Thermodynamic Properties

Radial profiles of thermodynamic variables (temperature, density, pressure, entropy, and cooling time) are essential tools for investigating cooling, feedback, and the thermodynamic state of clusters. In order to build such profiles, we extracted the spectra of circular annuli centered on the AGN and extending between $1\farcs5$ and $100''$ (7.5–500 kpc). The width of each annulus is designed to obtain more than 8000 counts in the 0.5–7 keV band, enabling us to constrain temperatures with an accuracy of 5% (8% when deprojected). The spectra were fit with a projected (tbabs*apec) and a deprojected (projct*tbabs*apec) thermal model.
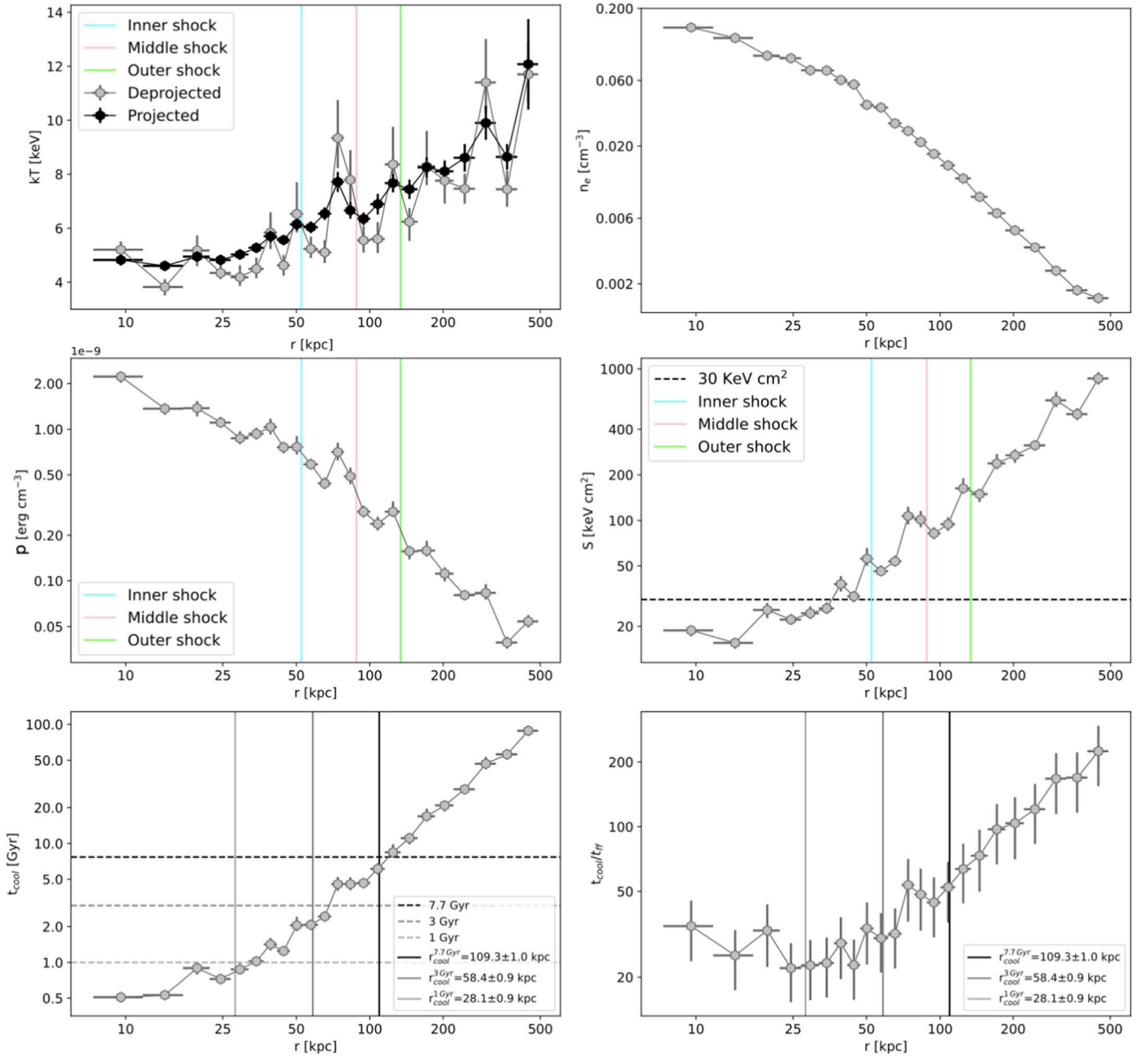
We show the resulting radial profiles of temperature (projected in black and deprojected in gray), density, pressure, entropy, and cooling time (estimated using Equations (1)–(4)) in the first five panels of Figure 3. We verified that neither intrinsic absorption (ztbabs*tbabs*apec) nor an additional thermal component (tbabs*(apec+apec)) is required in any of the annuli. We also checked that using the DSDEPROJ code (Sanders & Fabian 2007; Russell et al. 2008) to derive deprojected quantities returns consistent results with those obtained by using projct (see Figure B2).

The inwardly increasing density and decreasing temperature, entropy, and cooling time confirm that RBS 797 is a cool core cluster (as already noticed by Schindler et al. 2001; Bîrzan et al. 2004; Gitti et al. 2006; Cavagnolo et al. 2011; Doria et al. 2012). With our deeper exposure, we are now able to resolve localized gradients in thermodynamic properties. On the temperature, pressure, and entropy profiles, we overplot the distance from the center of the three nested shocks. Both the projected and deprojected temperature profiles reveal an increase in temperature behind the three edges; moreover, the pressure and entropy within the edges are higher than outside.

The radial spectral analysis allows us to characterize the efficiency of ICM cooling in RBS 797. First of all, we aim at determining the extent of the cool core region, usually defined in the literature as the region where the gas has a cooling time of less than 7.7 Gyr (corresponding to the look-back time of $z \sim 1$ for the assumed cosmology; Bîrzan et al. 2004). Other studies instead consider more conservative thresholds, such as 1 or 3 Gyr (typical timescale from the last major merger; e.g., McDonald et al. 2018). Thus, we fitted the cooling time profile with a power law and located the intersection with $t_{cool} = 1$, 3, and 7.7 Gyr. We find that the cooling radius (where cooling time is less than 7.7 Gyr[14]) in

---

[14] We are aware that for RBS 797 ($z = 0.354$), the time that has passed since $z = 1$ is not 7.7 Gyr but ~ 4 Gyr. However, a $t_{cool} \leqslant 7.7$ Gyr is the typical approach of several studies in the literature (e.g., Bîrzan et al. 2004; Rafferty et al. 2006) and has also been adopted for studies of clusters at higher redshift than RBS 797, up to $z \sim 1.2$ (e.g., Hlavacek-Larrondo et al. 2012, 2015; Bîrzan et al. 2017). Thus, using this threshold—while possibly nonphysical—enables us to draw comparisons with the literature.
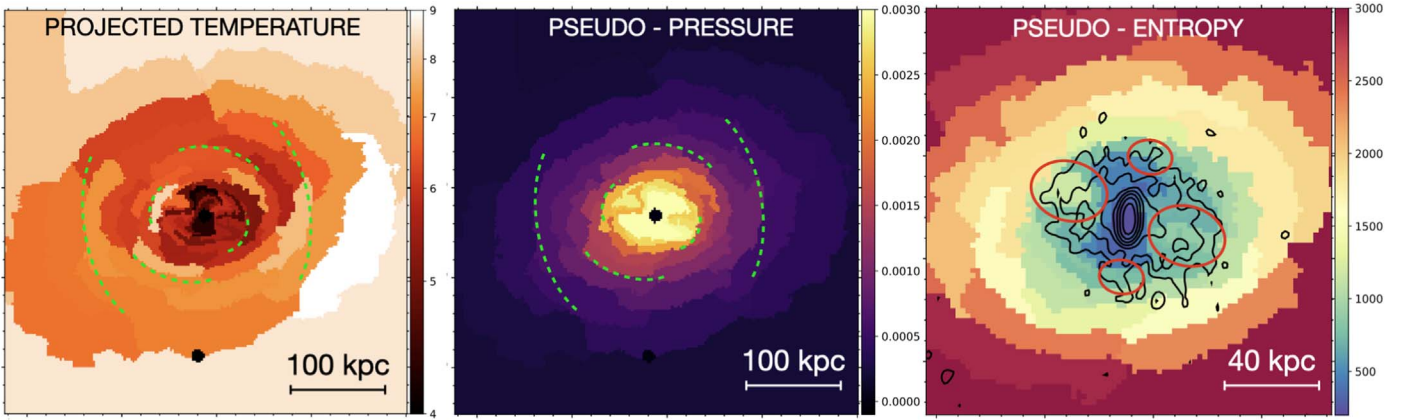
Figure 3. Radial profiles of ICM thermodynamic quantities in RBS 797. Upper left: projected (black dots) and deprojected (gray dots) temperature profiles. Upper right: electron density profile. Middle left: pressure profile. Middle right: entropy profile, with the horizontal dotted line showing the $S \leqslant 30$ keV cm^2 threshold for the condensation of the ICM into multiphase gas clouds. Lower left: cooling time profile, with horizontal lines showing different indicators (1, 3, and 7.7 Gyr) of the cool core region, the extent of which for each indicator is marked by the vertical lines. Lower right: radial profile of the ratio between the cooling time and the freefall time (t_{cool}/t_{ff}), with the different estimates for the cooling radius overlaid with vertical lines. In the temperature, pressure, and entropy profiles, the colored vertical lines show the distance from the center of the three nested weak shocks (see Section 3). For details on how these profiles were built, see Section 4.1.

RBS 797 is $r_{cool}^{7.7\,Gyr} = 109.3 \pm 1.0$ kpc (or 22″4—consistent with Doria et al. 2012). The cooling time falls below 3 Gyr within 58.4 ± 0.9 kpc and below 1 Gyr within 28.1 ± 0.9 kpc. Second of all, we wish to locate the radial range over which the ICM is not only cooling, but multiphase gas is also expected to be present. To fulfill this aim, we employed different ICM cooling diagnostics. On the one hand, according to McNamara et al. (2016), the gas should become multiphase when the entropy is lower than 30 keV cm^2 or the cooling time falls below 1 Gyr. As can be seen in Figure 3, these conditions are both satisfied within roughly 30 kpc from the center. On the other hand, it has been suggested that cooling of the ICM into

warm clouds occurs when the ratio between the cooling time and the freefall time (t_{ff}) is of the order of a few tens (10–30; e.g., Voit & Donahue 2015). To measure the freefall time, we derived the hydrostatic mass (e.g., Voigt & Fabian 2006) of RBS 797 from the deprojected pressure and density profile (as anticipated in Ubertosi et al. 2021). Then, from the mass profile $M(r)$, it is possible to obtain the freefall time profile as

$$t_{ff}(r) = \sqrt{\frac{2r^3}{GM(r)}}. \tag{11}$$

Figure 4. Maps of projected temperature (in keV; left panel), pseudopressure (in arbitrary units; middle panel), and pseudoentropy (in arbitrary units; right panel). The spectrum extracted from each region has an S/N $\geqslant$ 60. Relative uncertainties on the mapped values are $\leqslant$20%. In the left and middle panels, the green dashed arcs indicate the position and extent of the arc-like edges identified in Section 3. In the right panel, the black contours show the radio galaxy at 1.4 GHz (see Gitti et al. 2006), while the red ellipses indicate the X-ray cavities. The central X-ray point source has been excluded from the spectral fitting.

We show in Figure 3 the radial profile of $t_{\rm cool}/t_{\rm ff}$, which reveals that the ratio approaches $\sim$20–30 below $\sim$35 kpc from the center, which is also the extent of gas with $S \leqslant 30 \, {\rm keV \, cm^2}$ and $t_{\rm cool} \leqslant 1 \, {\rm Gyr}$. Therefore, in RBS 797, we find that the conditions for the presence of multiphase gas are met within a few tens of kiloparsecs from the center.

We note that the azimuthally averaged radial analysis can predict the extent of the region where condensation should occur but does not provide information on the azimuthal geometry of cold and dense gas. Thus, in the following subsection, we show different methods for building maps of ICM thermodynamic quantities that can provide valuable information on the radial and azimuthal variations of thermodynamic quantities and cooling efficiency.

4.2. Thermodynamic Maps of the ICM

To enable high-resolution 2D mapping of ICM thermodynamic properties, we built maps by using the contour binning technique (CONTBIN; Sanders 2006) and setting a minimum signal-to-noise ratio (S/N) of 60. The spectrum extracted from each region was fit with a tbabs*apec model, leaving the temperature, metallicity, and normalization free to vary. As done for the radial profile described in Section 4.1, we verified whether the inclusion of intrinsic absorption or the fit with a two-temperature model could improve the description of the extracted spectra, but we found that no additional component is required.

Then, by combining the temperature and normalization, we derived maps of pseudopressure and pseudoentropy in arbitrary units using the following method. The apec normalization is proportional to the volume integral of the square of the electron density, i.e., norm $\propto \int n_{\rm e}^2 \, dV$. Thus, the average projected electron density can be derived from the square root of the apec normalization scaled by a factor that accounts for the volume. We define this factor as $R \times n_{\rm pix}$, where R is the average distance of the spectral region from the center, and $n_{\rm pix}$ is the number of pixels in each spectral region (see also, e.g., Rossetti et al. 2007; Blanton et al. 2011; Randall et al. 2015). Therefore, we measure the pseudoelectron density using the

following proportion:

$$n_{\rm e} \propto \left(\frac{\rm norm}{R \times n_{\rm pix}} \right)^{1/2}. \qquad (12)$$

From the pseudodensity, it is trivial to measure pseudopressure and pseudoentropy using Equations (2) and (3). The resulting maps (shown in Figure 4) show that the cooler and lower-entropy gas is preferentially found in the bright central bar oriented N–S and the rims of the four X-ray cavities. These low-entropy structures are likely the result of the combined expansion of the four X-ray cavities in the ICM that may have uplifted the surrounding low-entropy medium and/or triggered its condensation. By overlaying the arcs representing the shock fronts discussed in Section 3 on the thermodynamic maps, it is possible to appreciate the presence of high-temperature and high-pressure regions behind the arcs. Additionally, the entropy map shows that the low-entropy gas encasing the X-ray cavities is more extended to the W. This supports the idea that low-temperature gas projected in front of S2 may be damping the temperature gradient, as hypothesized in Section 3.1.

Overall, the radial and thermodynamic map analysis revealed that the ICM of RBS 797 presents several radial and azimuthal gradients in spectral properties. In order to further investigate these features with improved statistics, and with the aim of measuring deprojected thermodynamic quantities at different radii and orientations, we performed a spectral mapping in annular sectors. In particular, we divided the azimuth into four sectors with angular apertures of 90°, starting in the W, with a center line at P.A. 345° for the first sector (to match the approximate symmetry of the central region). Then, each sector was divided into nine annular regions, so that each annular sector contained at least the same number of counts (8000 in the 0.5–7 keV band) as the annuli used to construct the radial profiles in Figure 3. By fitting the spectra with a projct*t-babs*apec model, we are thus able to probe radial and azimuthal variations of deprojected thermodynamic properties (see also Gitti et al. 2010). To derive useful information on the distribution of cooling gas, we also mapped the cooling time and $t_{\rm cool}/t_{\rm ff}$ ratio by measuring the freefall time at the radial distance of each annulus from the center (Equation (11)).
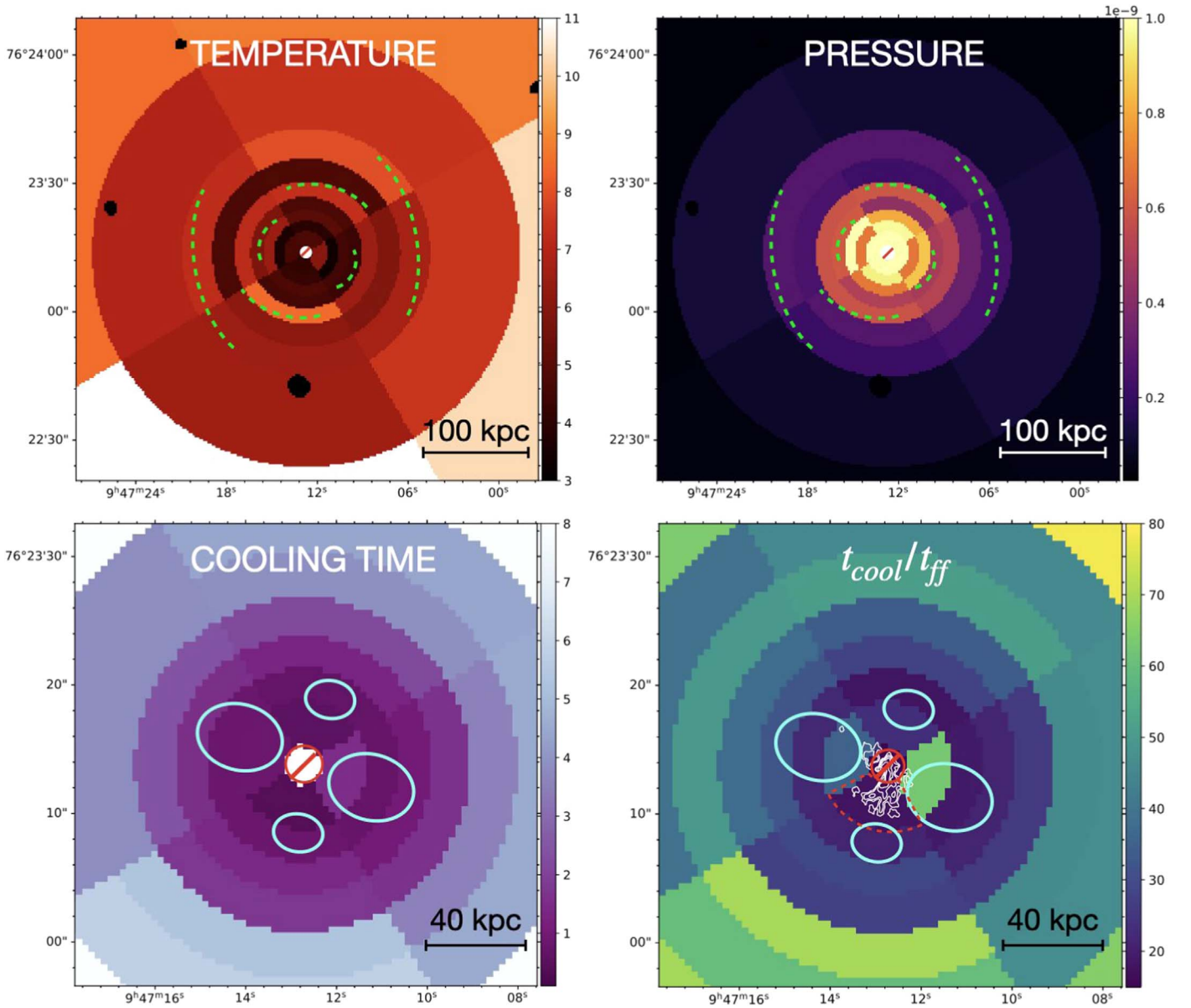
Figure 5. Maps of deprojected temperature (upper left; in keV), pressure (upper right; in erg cm^{-3}), cooling time (lower left; in Gyr) and t_{cool}/t_{ff} ratio (lower right) of the ICM, built by dividing the azimuth into four sectors and nine annuli (see text for details). In the upper panels, the green dashed arcs indicate the position and extent of the arc-like edges identified in Section 3. In the lower panels, cyan ellipses show the positions of the X-ray cavities. In the lower right panel, white contours from Calzadilla et al. (2022) trace the morphology of the central [O II]-emitting nebulae, and the red dashed wedge shows the region where the minimum in t_{cool}/t_{ff} is found. Relative uncertainties in temperature, pressure, and cooling time are on the order of $\sim$10%, while those in t_{cool}/t_{ff} are on the order of $\sim$20%. The central X-ray point source has been excluded from the spectral fitting.

The resulting deprojected temperature and pressure maps (see Figure 5) highlight the concentric, nested, and misaligned weak shocks (as found in the projected thermodynamic maps of Figure 4). We note that due to the choice of circular symmetry and the fact that the wedges do not exactly follow the shock fronts, the outer jump is less well defined.

The cooling time and t_{cool}/t_{ff} maps (lower panels in Figure 5) confirm that short cooling time ($\leqslant$1 Gyr) gas is filling the space between and around the perpendicular radio lobes and cavities, supporting a strong connection between the AGN outbursts and ICM cooling. We note that the innermost southern wedge (red dashed region in Figure 5) represents the locus where cooling should be most effective; we measure a local cooling time of $t_{cool} = 438 \pm 51$ Myr and $t_{cool}/t_{ff} = 17.9 \pm 2.0$ (and an entropy

$S = 15.4 \pm 1.2$ keV cm^2, not shown here). We thus expect that filamentary multiphase warm gas arising from condensation of the ICM should preferentially be found in this region. In this context, Cavagnolo et al. (2011) noted filamentary structures in the residual optical image of the BCG extending 8–10 kpc southward. These structures were recently confirmed by Calzadilla et al. (2022), who produced continuum-subtracted [O II] maps of nebular emission using the Hubble Space Telescope. The overlay of [O II] contours on the t_{cool}/t_{ff} map (see lower right panel in Figure 5) reveals that cool gas at $\sim$10^4 keV is coincident with the region where the minimum in t_{cool}/t_{ff} is found (within $\sim$20 kpc S from the center). These results may indicate that the local ICM is actually condensing into cool gas.

4.3. Metallicity of the ICM

A previous study of the metallicity distribution based on the analysis of the ∼50 ks exposure found tentative indications of higher abundances in the direction of the E–W cavities compared to the surrounding medium (Doria et al. 2012), possibly suggesting that the thrust associated with the cavities' expansion was uplifting enriched gas from the center, as seen in a number of other systems (e.g., Kirkpatrick et al. 2011; Kirkpatrick & McNamara 2015). Our aim is to follow up on this argument with the deeper Chandra exposure by analyzing the radial and azimuthal distribution of metals in RBS 797.

Constraining the abundances of the ICM with Chandra typically requires spectra with a high S/N ($\gtrsim$100). Therefore, to map the ICM abundances, we built another set of maps requiring a minimum S/N of 100 in the 0.5–7 keV band for each spectral extraction region. Fitting the spectra with a `tbabs*apec` model allowed us to map abundances with relative uncertainties of $\leqslant$10%–15%. The metallicity map obtained with this choice of S/N is shown in Figure 6. We note that within the inner ∼50–70 kpc, the abundance is higher than outside ∼80 kpc from the center, which is expected in a cool core cluster. A peculiar feature in the metallicity map is the presence of a ring of enhanced metallicity at ∼50 kpc from the center. By overlaying 1.4 GHz radio contours on the map, it is possible to see that this ring surrounds the lobes of the central radio galaxy to the E, N, W, and SW of the center. On the one hand, this feature is consistent with the scenario proposed by Doria et al. (2012) that the AGN is responsible for mechanical uplift of enriched gas from the center. On the other hand, the deep Chandra exposure seems to rule out a bipolar uplift, as the ring covers almost the whole azimuth. In fact, the discovery of four equidistant cavities excavated by the AGN in perpendicular directions (Ubertosi et al. 2021) is consistent with an azimuthally symmetric enhancement. This has also been predicted by high-resolution hydrodynamical simulations of AGN jet feedback (e.g., Gaspari et al. 2011).

We note that both the analysis of Doria et al. (2012) and the metallicity map shown in Figure 6 do not take into account projection effects. Measuring accurate deprojected abundances requires an even larger S/N. Thus, to build a high-fidelity radial profile of abundances, we extracted the spectrum from nine concentric circular annuli (extending between 1″5 and 100″ from the center) centered on the AGN, requiring ∼30,000 counts bin^{-1} (or S/N ∼ 200). By again fitting the spectra with a `tbabs*apec` model, we verified that the relative uncertainties on the projected and deprojected abundances are ∼6% and ∼10%–15%, respectively. The projected and deprojected profiles shown in Figure 6 confirm the general decreasing trends of abundances with radius; there is a clear gradient at roughly 80 kpc from the center, with average (deprojected) abundances of $\langle Z(r \leqslant 80\,\mathrm{kpc})\rangle = 0.62 \pm 0.04$ and $\langle Z(r \geqslant 80\,\mathrm{kpc})\rangle = 0.41 \pm 0.05\ Z_\odot$. Furthermore, the projected and deprojected profiles hint at a slightly lower central abundance (by approximately 15%) than in the region where the X-ray cavities are located (20–50 kpc; overplotted in green). As a sanity check, we tested whether our results could be affected by the iron bias (see, e.g., Buote 1999) by fitting a two-temperature model to the spectra of the nine radial bins, finding that the plasma is well described by a single-temperature model; thus, we conclude that the abundances

are not being underestimated. We also exclude that the inverse iron bias (see, e.g., Gastaldello et al. 2010) is responsible for the higher abundance at the cavity edges, as this effect is typical of clusters with temperatures of 2–4 keV, while RBS 797 has temperatures that do not fall below 4 keV (see Section 4.1). We thus conclude that the Chandra data hint at a slight excess in metallicity between 20 and 50 kpc with respect to the central gas, which may be due to the AGN pushing enriched gas outward while inflating its radio lobes.

5. The Central X-Ray Point Source

At the center of the Chandra image of RBS 797, there is a bright X-ray point source that coincides with the radio core of the AGN. Given its location, this point source likely represents the nonthermal X-ray emission from the nucleus of the radio galaxy. Indeed, the study of the previous Chandra exposures found that the X-ray source is well described by an absorbed power law (Cavagnolo et al. 2011). To measure its properties with our deeper X-ray observations, we extracted the spectrum of a circle with radius 1″5 (∼7 kpc, which encloses 90% of the encircled energy fraction) centered on the source. The background spectrum was extracted from an annulus extending between 2″ and 6″ from the center. The resulting source spectrum has roughly 5000 net counts in the 0.5–7 keV band.

As also observed by Cavagnolo et al. (2011), we found that the spectrum has the typical appearance of a slightly absorbed power law. There are no indications of the presence of residual thermal components possibly related to the central ICM, suggesting that the plasma properties between 2″ and 6″ (the local background extraction region) and those within 1″5 from the center are similar (see also the rather flat temperature and metallicity profiles of Perseus in this radial range; e.g., Schmidt et al. 2002; Fabian et al. 2006). Using a Galactic-absorbed power-law model (`tbabs*po`, without intrinsic absorption) to describe the spectrum results in a rather poor fit; the unphysically flat power-law index ($\Gamma = 0.31 \pm 0.04$) and the $\chi^2/\mathrm{d.o.f.} = 548.6/373 = 1.47$ indicate that an additional component is likely required. Indeed, adding an intrinsic absorber (`ztbabs`) at the cluster redshift of 0.354 resulted in a good fit; we find a modest intrinsic column density of $N_{\mathrm{H}}^{\mathrm{int}} = (7.49 \pm 0.82) \times 10^{22}\ \mathrm{cm}^{-2}$ and power-law index $\Gamma = 1.70 \pm 0.12$ for a $\chi^2/\mathrm{d.o.f.} = 385.9/372 = 1.03$. The improvement is thus statistically significant (F-test value of 156.8 and null-hypothesis probability 2×10^{-30}).

The value of $N_{\mathrm{H}}^{\mathrm{int}}$ is consistent with previous estimates (Cavagnolo et al. 2011) and suggests that the AGN is not heavily obscured. The steep power-law index is typical of radio galaxies in BCGs; converting the power-law index to a spectral index ($\alpha_X = \Gamma - 1 = 0.7$), we find a good agreement with the spectral index measured at gigahertz radio frequencies ($\alpha_R \sim 0.9$; Gitti et al. 2006). The 2–10 keV power-law luminosity is $L_{2-10\,\mathrm{keV}} = (1.37 \pm 0.04) \times 10^{44}\ \mathrm{erg\ s}^{-1}$, while the bolometric power-law luminosity is $L_{\mathrm{bol}}^{\mathrm{X}} = (4.18 \pm 0.02) \times 10^{44}\ \mathrm{erg\ s}^{-1}$. The 2–10 keV and 5 GHz luminosities of the unresolved radio core of the AGN ($5.4 \times 10^{40}\ \mathrm{erg\ s}^{-1}$; Gitti et al. 2006) can be combined to estimate the mass of the SMBH in RBS 797 using the fundamental black hole plane (Gültekin et al. 2019), obtaining $M_{\mathrm{BH}} \sim 1.4 \times 10^9\ M_\odot$. This value is in good agreement with the
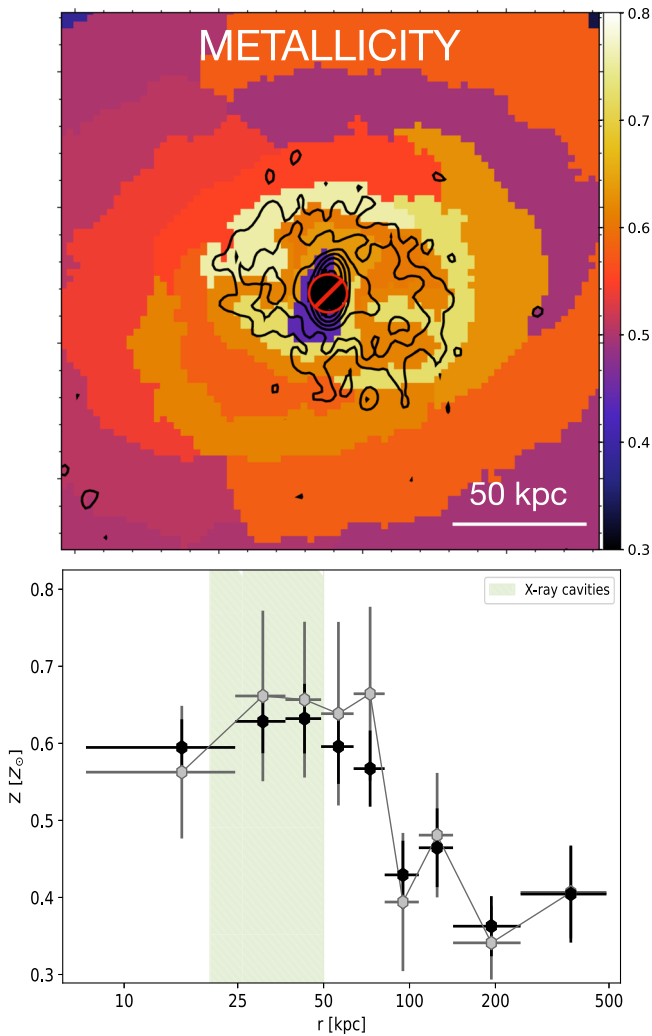
Figure 6. Upper panel: metallicity map of the ICM in $Z_\odot$. The spectrum extracted from each region has an $S/N \sim 100$. Relative uncertainties on the mapped values are $\leqslant 10\%$–15%. Overlaid in black are the contours of the radio galaxy at 1.4 GHz (same as in Figure 1; Gitti et al. 2006). The central X-ray point source has been excluded from the spectral fitting. Lower panel: projected (black dots) and deprojected (gray dots) metallicity radial profile, with the green shaded region showing the radial range where the X-ray cavities are located.

estimate of $M_{\mathrm{BH}} \sim 1.5 \times 10^9 \, M_\odot$ based on the central velocity dispersion (Cavagnolo et al. 2011).

6. Discussion

The three weak shocks propagating in the ICM indicate that AGN feedback in RBS 797 has perturbed the environment. The discovery of shocks in ellipticals, groups, and clusters has been limited mainly because of the large exposures typically needed to detect such features, and only a few tens of objects with weak shocks due to AGN activity are known. The number of known systems with multiple shock fronts is even lower (M87, Forman et al. 2017; A2052, Blanton et al. 2009; and NGC 5813, Randall et al. 2015), making RBS 797 the fourth object known to have more than one shock and the farthest in redshift. Coupled with the presence of multiple X-ray cavities in its cool core (Schindler et al. 2001; Cavagnolo et al. 2011; Doria et al. 2012; Ubertosi et al. 2021), this makes RBS 797 one of the rare windows to investigate feedback history and ICM heating in clusters.
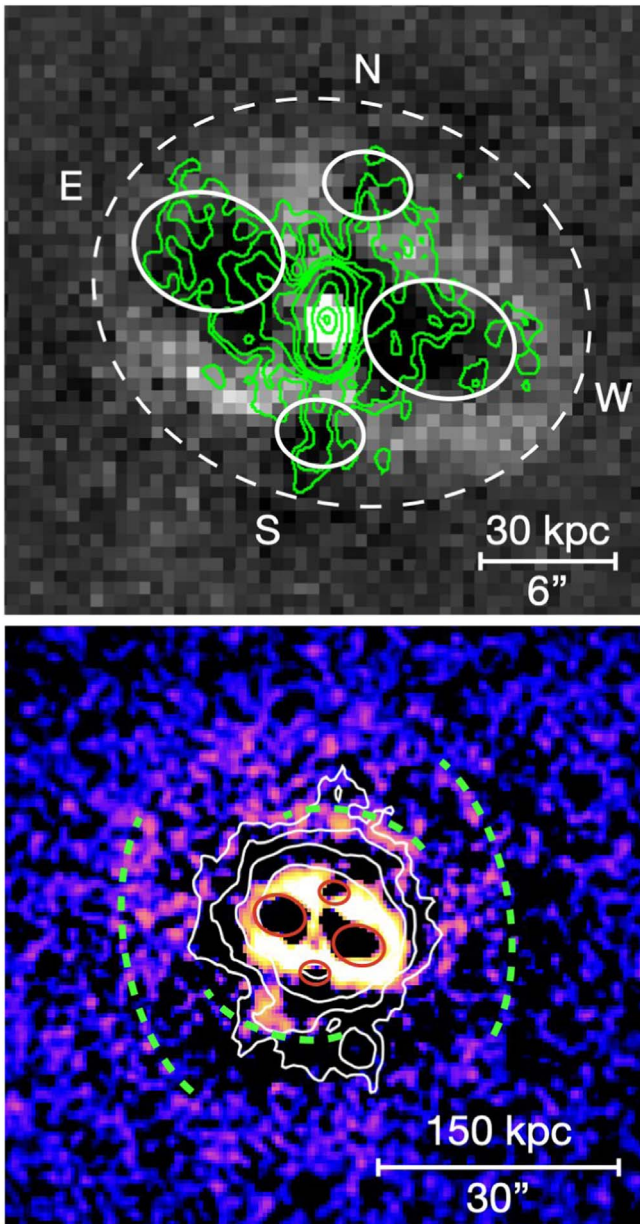
6.1. The Episodic AGN Feedback in RBS 797

The analysis of the weak shocks in RBS 797 (Section 3) revealed that the power released by the AGN in shocks has not changed drastically between outbursts, injecting roughly 10^{61} erg about every 25 Myr. We now aim to perform a similar evaluation for the four X-ray cavities at the center of RBS 797. The first results from the deep exposure indicated that the two pairs of cavities on perpendicular axes have similar ages (around $\sim$30 Myr; Ubertosi et al. 2021). The preliminary analysis of our new JVLA data (F. Ubertosi et al. 2023, in preparation) further supports the existence of the four cavities, as the 3 GHz radio contours (Figure 7, top panel) are found for the first time to also nicely fill the newly discovered N–S cavities.

To determine the energetics of the four X-ray cavities (whose shape is shown with white ellipses in Figure 7), we consider that $H = [\gamma/(\gamma - 1)]pV = 4pV$ (assuming $\gamma = 4/3$) is the enthalpy of a cavity (where p is the pressure of the surrounding ICM, and V is the cavity volume), which is also the minimum total energy required to inflate the cavity (e.g., Bîrzan et al. 2004). From the pressure profile shown in Figure 3, we find an ICM pressure at the average distance of the cavities from the center ($\sim$27 kpc) of $p = 9.7 \pm 0.8 \times 10^{-10}$ erg cm^{-3}. The volumes have been determined from the sizes reported in Table 1 of Ubertosi et al. (2021) by assuming that the cavities are prolate ellipsoids and including a 10% relative uncertainty. The results are reported in Table 2. Then, to compute the cavity power $P_{\mathrm{cav}} = E_{\mathrm{cav}}/t_{\mathrm{age}}$, we considered the age estimates we derived in Ubertosi et al. (2021). To account for the different methods used to determine the age of each cavity (sound speed, buoyancy, refill, and expansion timescale; see, e.g., McNamara & Nulsen 2012), we computed the mean of the four values for each cavity (column (3) in Table 2), assuming the scatter as an estimate of our uncertainty (which is larger than the statistical errors). The similar ages of the bubbles are compatible with the E–W and N–S X-ray cavities being nearly coeval (Ubertosi et al. 2021).

Overall, the difference in power between the E–W ($\sim$3 × 10^{45} erg s^{-1}) and N–S ($\sim$6 × 10^{44} erg s^{-1}) cavity pairs reflects the difference in energy (a factor of 5), which in turn is caused by the E–W cavities being larger than the N–S ones. In Ubertosi et al. (2021), we argued that the nearly coeval cavities are consistent with both a rapid reorientation of the AGN jets and the presence of binary AGNs in the BCG. Both scenarios may account for the different power; either the AGN has reoriented its jets and reduced/increased its mechanical power (see also, e.g., MS 0735.6+7421; Vantyghem et al. 2014), or the X-ray cavities might have been excavated by two AGNs with different mechanical power.

By summing the values of each cavity (Table 2; column (2) for energy and column (4) for power), we deduce that the total energy stored in the four X-ray cavities is $E_{\mathrm{cav}}^{\mathrm{tot}} = 3.3 \pm 0.5 \times 10^{60}$ erg, while the total power is $P_{\mathrm{cav}}^{\mathrm{tot}} = 3.6 \pm 2.2 \times 10^{45}$ erg s^{-1}. By comparing these values with the total energy carried by shocks, we find that $E_{\mathrm{sh}}^{\mathrm{tot}}/E_{\mathrm{cav}}^{\mathrm{tot}} \sim 18$. This value is slightly higher than those of other galaxy clusters and groups with shocks and X-ray cavities, where the $E_{\mathrm{sh}}/E_{\mathrm{cav}}$ ratio ranges between 0.1 and 10 (Liu et al. 2019). It is worth mentioning, however, that if we are missing older X-ray cavities associated with the middle and outer shocks, then the ratio obtained for RBS 797 might be overestimated. It is useful to compare RBS 797 with the galaxy group NGC 5813, where

Table 2
Energetics of the Four X-Ray Cavities in RBS 797

(1)	E_{cav} $(10^{60}$ erg) (2)	t_{age} (Myr) (3)	P_{cav} $(10^{45}$ erg s$^{-1})$ (4)
Cavity E	1.4 ± 0.2	30.9 ± 15.6	1.4 ± 0.9
Cavity W	1.4 ± 0.2	29.5 ± 16.2	1.5 ± 0.9
Cavity N	0.29 ± 0.04	29.2 ± 13.3	0.32 ± 0.17
Cavity S	0.29 ± 0.04	27.7 ± 12.9	0.34 ± 0.18

Note. (1) Cavity name (see Figure 1 in Ubertosi et al. 2021; see also Figure 7). (2) Energy of the cavity, computed as $E_{cav} = 4pV$ (see text for details). (3) Age of the X-ray cavity, computed as the average of the sound cross, buoyancy, refill, and expansion timescales reported in Table 1 of Ubertosi et al. (2021). (4) Cavity power $P_{cav} = E_{cav}/t_{age}$.

misaligned cycles of AGN activity in RBS 797 determined a complex ICM geometry, which in turn prevents us from clearly linking X-ray cavities and shocks.

In this context, we note the good agreement between the age of the E–W/N–S cavities ($\sim$28–31 Myr) and the age of the inner edge ($t_{age}^{S_{in}} = 33.4 \pm 1.3$ Myr). This similarity in timescales further strengthens the association between the X-ray cavities and the inner shock already evident in the morphology. Furthermore, we may speculate that the inner shock, being stronger in the E–W direction (see Section 3.1), has been driven by the same jet episode that inflated the E–W X-ray cavities. This hypothesis could suggest that the N–S cavities are younger than the E–W ones (by a factor smaller than our uncertainties, which points to the cavities being nearly coeval; see Table 2 and the discussion in Ubertosi et al. 2021), since otherwise, the inner cocoon shock would have disrupted any previous N–S small bubble (see, e.g., the example of M87 in Churazov et al. 2001). However, projection effects may hide the true 3D distribution of the cavities within the cocoon shock, which in turn prevents us from drawing firm conclusions on which jet activity episode is responsible for the inner shock front. Moreover, even though the N–S cavity power indicates a weaker outburst with respect to the E–W one, the N–S jet activity may also have driven weak shock waves that we are unable to detect. Indeed, any AGN jet episode can drive weak shocks, regardless of the jet power (see the simulations of Bourne & Sijacki 2021), with shocks driven by weaker jets quickly broadening into sound waves (which are difficult to detect even in local, deeply observed clusters; see, e.g., Graham et al. 2008a).

Regarding the middle and outer shocks, the detection of other, external X-ray cavities is likely prevented by the increasing difficulty in detecting cavities at large distances from the center (e.g., Bîrzan et al. 2009) and the complicated geometry of the cluster. For instance, older cavities produced $\sim$80 Myr ago (when the outer shock was launched) may have been overridden and distorted by the passage of the middle shock $\sim$54 Myr ago (see also Bogdán et al. 2014). In this respect, we notice that RBS 797 shows diffuse radio emission within its cool core, with an extent of $\approx$100 kpc and slightly elongated to N–S. The diffuse radio source has been classified as a radio minihalo (Gitti et al. 2006; Doria et al. 2012). Without entering a detailed discussion, we may speculate a connection between the mechanical power driven by the AGN activity in the ICM and the diffuse radio emission. Shocks may

Figure 7. Residual Chandra images of RBS 797. Upper panel: zoom on the inner $\sim$60 kpc. The four white ellipses and corresponding labels indicate the shape and name of the X-ray cavities. The dashed white ellipse traces the inner cocoon shock. Green contours at 3 GHz from the new JVLA observations (see Section 2.2; F. Ubertosi et al. 2023, in preparation) are overlaid. The resolution is $0''.9 \times 0''.8$, the rms noise is 5 μJy beam^{-1}, and the contours are drawn at (6, 8, 10, 12, 16, 48, 96, 256, 360) $\times$ rms. Lower panel: residual image of the inner $\sim$300 kpc. Green dashed arcs mark the position of the middle and outer shock fronts. White contours at 1.4 GHz from the VLA (3$''$ resolution; see Section 2.2 for details) show the diffuse radio emission surrounding the AGN (see Doria et al. 2012).

Randall et al. (2011, 2015) found three collinear pairs of X-ray cavities, each associated with an elliptical shock front. First, it is interesting to note that both NGC 5813 and RBS 797 have an outburst repetition rate of one shock every $\approx 2 \times 10^7$ yr. Thus, at least for these two examples, we observe that the repetition interval of low-mass systems is similar to that of high-mass systems. Nonetheless, while in NGC 5813, the alignment of the outbursts enables a clear association of each X-ray cavity system with its shock, the

(re)accelerate relativistic seeds from AGN outbursts via several mechanisms, including compression and turbulence (generated downstream by the shocks themselves), and advect the plasma on 100 kpc scales (e.g., Brunetti & Jones 2014). By over-plotting the 1.4 GHz VLA radio contours on the Chandra residual image in the lower panel of Figure 7, we notice that the N–S radio protrusions are roughly parallel to the axis of the outer shock, while the roundish structure outside the cavities seems to be caged within the middle shock. It may thus be possible that we are observing the remnant of what once were distinct AGN outbursts in several directions; due to the passage of multiple shocks, the radio emission may have been distorted until a rather amorphous and nearly circular shape had formed.

6.2. Are Heating and Cooling Balanced in RBS 797?

To test the ICM–AGN feedback cycle paradigm, we aim at comparing the shock and cavity powers with the amount of radiative losses in the X-ray band. Several studies in the literature have considered that the gas bolometric X-ray luminosity within the cooling radius of cool core clusters can be considered as a proxy for the magnitude of ICM cooling and flowing to the center (e.g., Fabian et al. 1984; Bîrzan et al. 2004; Rafferty et al. 2006).

We determined that RBS 797 has a cool core (where $t_{cool} \leqslant 7.7$ Gyr) with a cooling radius of 109 kpc (see Section 4.1). We thus extracted the spectrum of the gas within the cooling radius (excluding the inner $1''5$) and of the region between 109 and 500 kpc to allow for deprojection. The spectra were fitted with a deprojected thermal model (`projct*tbabs*apec`), obtaining the following results.

1. For $r \leqslant r_{cool}$, the ICM has a temperature $kT = 5.55^{+0.03}_{-0.05}$ keV and an abundance $Z = 0.56 \pm 0.02$ $Z_\odot$ and radiates a bolometric luminosity of $L^X_{bol} \equiv L_{cool} = (2.34 \pm 0.01) \times 10^{45}$ erg s^{-1}.
2. For $r > r_{cool}$, we measure a temperature $kT = 8.28 \pm 0.12$ keV, an abundance $Z = 0.40 \pm 0.03$ $Z_\odot$, and a bolometric luminosity $L^X_{bol} = (1.45 \pm 0.02) \times 10^{45}$ erg s^{-1}. The χ^2/d.o.f. is 5896/6012 (=0.98).

We also tested the inclusion of an isobaric cooling component (`mkcflow`) to constrain the spectroscopic mass deposition rate, i.e., the rate at which gas is actually cooling to lower temperatures, by fitting a `tbabs*(apec+mkcflow)` model to the spectrum of the ICM for $r \leqslant r_{cool}$. The high temperature and abundance of the `mkcflow` component were tied to the values of the `apec`, while the low temperature was fixed at 0.1 keV. We found that we can only place an upper limit on the mass deposition rate of $\dot{M}_{cool} \leqslant 37$ $M_\odot$ yr^{-1} (at 99% confidence). By reducing the size of the extraction region to $r \leqslant 30$ kpc (where the entropy is smaller than 30 keV cm^{-2}; see Section 4.1), we still measure an upper limit on the mass deposition rate of $\dot{M}_{cool} \leqslant 40$ $M_\odot$ yr^{-1}. We note that Doria et al. (2012) obtained $\dot{M}_{cool} = 231^{+316}_{-227}$ $M_\odot$ yr^{-1} from the previous Chandra observations. While this estimate would suggest a much higher mass deposition rate, the associated large uncertainties are fully consistent with our more stringent upper limit.

Altogether, we find that cavity power alone ($P^{tot}_{cav} = 3.6 \times 10^{45}$ erg s^{-1}) can balance radiative losses within the cool core of RBS 797. Including the energy injected in shocks, the total heating power of the AGN in RBS 797 is roughly 3.4×10^{46} erg s^{-1}, which exceeds the cooling luminosity,

$L_{cool} = (2.34 \pm 0.01) \times 10^{45}$ erg s^{-1}, by a factor of $\sim$14. Additionally, we note that the outer shock, which is located $\sim$130 kpc from the center, lies outside the cool core ($r_{cool} \sim 109$ kpc). Thus, the AGN in RBS 797 may be able to not only match radiative losses within the cool core but also heat the gas at larger distances from the center. Similar results were obtained in the cases of Hydra A (e.g., Nulsen et al. 2005; Wise et al. 2007) and MS 0735.6+7421 (e.g., McNamara et al. 2005; Gitti et al. 2007), where, however, giant cavities (with radii exceeding 100 kpc) and large-scale shock fronts (at distances of more than 200 kpc from the center) were found. The fact that in RBS 797, smaller shock fronts (and the possibly associated undetected cavities) lie outside r_{cool} may imply that heating beyond the cool core is more common than previously thought (i.e., there may be undetectable cavities and shock fronts or sound waves at $r \geqslant r_{cool}$ in many other systems).

We can also test the local balance of shock heating and radiative cooling. Following the strategy applied by Randall et al. (2011, 2015) to NGC 5813, we consider that the fractional effective heat input from one shock is $\Delta \ln(p/\rho^\gamma)$. Considering the Mach numbers of the shock fronts (see Table 1), we find that the change in $\ln(p/\rho^\gamma)$ across the inner, middle, and outer shocks is $\sim$1%, $\sim$0.4%, and $\sim$0.5%, respectively. Taking the reciprocal of these values, we find that $\sim$100, $\sim$250, and $\sim$200 outbursts are needed per local cooling time to completely offset cooling with shock heating at the location of the inner, middle, and outer shock edges, respectively. The cooling time outside the edges is 2 (inner shock), 5 (middle shock), and 9 (outer shock) Gyr. Assuming an outburst interval of 25 Myr (see Section 6.1) gives 80 (inner shock), 200 (medium shock), and 360 (outer shock) shocks per local cooling time. Thus, we find that in RBS 797, there is agreement between the number of shocks required to offset radiative cooling and those expected per local cooling time (as found by Randall et al. 2011, 2015 for the galaxy group NGC 5813).

6.3. Shock and Cavity Heating of Hot Atmospheres

The total AGN mechanical power in RBS 797 (which is larger than L_{cool} by a factor of $\sim$14) may seem extreme with respect to systems in typical samples of galaxy clusters, galaxy groups, and elliptical galaxies, where the average ratio between mechanical power and cooling luminosity is close to unity (e.g., Bîrzan et al. 2004; Rafferty et al. 2006). However, such samples are mostly composed of systems where only X-ray cavities have been found, whereas in RBS 797, we also consider the energy injected by shocks that dominates the AGN power. Indeed, by considering only the X-ray cavities, we find a ratio $P_{cav}/L_{cool} \sim 1$. Thus, a more consistent comparison should be made with other systems with detections of both X-ray cavities and weak shocks. Liu et al. (2019) assembled a compilation of 13 galaxy clusters, groups, and ellipticals in which X-ray cavities and shocks have been detected and for which Mach numbers, shock energies, and cavity energies are available. As we are interested in the comparison between the shock power, X-ray cavity power, average total (=shock + cavity) heating power, and cooling luminosity, first we verified that these 13 systems also have available measurements of such quantities. Additionally, we checked whether new detections had been claimed after the work of Liu et al. (2019), finding no new results. Surface brightness edges were identified in 3C 220.1

Table 3
Systems with X-Ray Cavities and Weak Shocks, Ordered by Decreasing X-Ray Cooling Luminosity

Name (1)	L_{cool} (10^{43} erg s^{-1}) (2)	P_{sh} (10^{43} erg s^{-1}) (3)	P_{cav} (10^{43} erg s^{-1}) (4)	P_{tot} (10^{43} erg s^{-1}) (5)	FR Class (6)	K_0 (keV cm^2) (7)	References (8)
RBS 797	234	2900	360	3360	FR I	20.0 ± 2.4	This work
Perseus	67	120	32	152	FR I	19.4 ± 0.3	1, 2
MS 0735.6+7421	26	1100	1700	2800	FR II	16.0 ± 3.2	3, 4
Hydra A	25	200	210	410	FR I	13.3 ± 0.7	1, 5, 6
Cygnus A	29	1000	210	1210	FR II	23.6 ± 0.9	1, 7, 8
A2052	8.4	1.0	3.2	4.2	FR I	9.5 ± 0.7	1, 9
3C 444	8.0	2900	61	2961	FR II	⋯	10, 11
Centaurus A	3.0	1.2	0.74	1.94	FR I	2.3 ± 0.1	1, 12, 13
3C 310	1.7	190	130	320	FR II	⋯	14
M87	0.98	2.4	1.0	3.4	FR I	3.5 ± 0.1	1, 15, 16, 17, 18
HCG 62	0.15	4.0	0.38	4.4	FR I	3.4 ± 0.1	19
NGC 5813	0.055	3.5	0.18	3.7	FR I	1.4 ± 0.2	20, 21
3C 88	0.055	10	2.0	12	FR II	7.3 ± 1.7[a]	22
NGC 4636	0.030	0.16	0.11	0.27	FR I	1.4 ± 0.1	23, 24, 25
NGC 4552	0.0025	0.33	0.015	0.35	FR I	⋯	26

Notes. (1) Name. (2) Cooling luminosity. (3) Total shock power. (4) Total cavity power. (5) Total heating power, defined as $P_{tot} = P_{cav} + P_{sh}$. (6) FR class of the central radio galaxy (based on radio morphology and/or power; see literature references in column (8)). (7) Central entropy from Cavagnolo et al. (2009), defined as the excess entropy above the best-fitting power law found at larger radii. (8) Literature references for the values reported in columns (2)–(6): [1] Bîrzan et al. (2004), [2] Graham et al. (2008b), [3] Vantyghem et al. (2014), [4] Biava et al. (2021), [5] Nulsen et al. (2005), [6] Wise et al. (2007), [7] Bîrzan et al. (2012), [8] Snios et al. (2018), [9] Blanton et al. (2009), [10] Croston et al. (2011), [11] Vagshette et al. (2017), [12] Rafferty et al. (2006), [13] Croston et al. (2009), [14] Kraft et al. (2012), [15] Churazov et al. (2001), [16] Forman et al. (2005), [17] Forman et al. (2007), [18] Forman et al. (2017), [19] Gitti et al. (2010), [20] Randall et al. (2011), [21] Randall et al. (2015), [22] Liu et al. (2019), [23] Jones et al. (2002), [24] O'Sullivan et al. (2005), [25] Baldi et al. (2009), [26] Machacek et al. (2006).
[a] The value is taken from Liu et al. (2019).

by Liu et al. (2020) and 3C 320 by Vagshette et al. (2019); however, due to the insufficient number of counts, a spectral confirmation of their shock front nature was not performed. We also consider Perseus due to the putative weak shock surrounding its inner X-ray cavities (Graham et al. 2008b). In Table 3, we report the properties of the 15 systems (13 from Liu et al. 2019 + Perseus + RBS 797) with the corresponding literature references. We find that RBS 797 has the largest cooling luminosity and total power among the 15 objects.

In the three panels of Figure 8, we plot the comparison of P_{cav} versus L_{cool}, P_{sh} versus L_{cool}, and P_{tot} versus L_{cool} for the objects we selected. The top panel reveals the trend already well tested (e.g., Bîrzan et al. 2004; Rafferty et al. 2006; Bîrzan et al. 2012) between the mechanical power of X-ray cavities and the cooling luminosity of the ambient gas. With a span in P_{cav} and L_{cool} of about 5 orders of magnitude, these 15 systems confirm that larger ICM radiative losses are accounted for by more powerful outbursts. In the middle panel, we show that the shock power also scales with the X-ray cooling luminosity, suggesting that the whole AGN mechanical output is set in response to the amount of available fuel. We note that the majority of the systems have $P_{cav}/L_{cool} \geqslant 1$ and $P_{sh}/L_{cool} \geqslant 1$ (dashed lines in the first two panels of Figure 8); given that shocks are more likely found for powerful objects, it is unsurprising that our selection criteria identify systems where cooling is largely balanced by mechanical feedback. These trends are consistent with the plot in the bottom panel, which shows the scaling between the total average heating power $P_{tot} = P_{cav} + P_{sh}$ and the cooling luminosity. As mentioned above, while RBS 797 has a high total mechanical power, it may not be an extremely heated object in a relative sense. Indeed, the high cooling luminosity of RBS 797 indicates a

ratio $P_{tot}/L_{cool} \sim 14$, whereas there are systems in the bottom panel of Figure 8 that are able to provide total mechanical power that exceeds the radiative losses of their gaseous halos by 2 orders of magnitude. In particular, we note that the upper area of the P_{tot}/L_{cool} space is populated by the 3C sources 3C 88, 3C 310, and 3C 444; Cygnus A; and MS 0735.6+7421, which have P_{tot}/L_{cool} ratios ranging between 50 (Cygnus A) and 370 (3C 444).

By considering the FR class of the radio galaxies in our compilation (see Table 3), we find that the sources named above are all FR II radio galaxies, while the other systems host FR I AGNs at their center, characterized by $0.5 \leqslant P_{tot}/L_{cool} \leqslant 60$. We note that this distinction also holds for the P_{cav}/L_{cool} and P_{sh}/L_{cool} comparison (top and middle panels of Figure 8). The two classes seem to overlap at $P_{tot}/L_{cool} \sim 50$–60, where we find that NGC 5813, a low-luminosity FR I radio galaxy, has a larger ratio than Cygnus A, the archetypal FR II radio galaxy. However, the different environments have to be taken into consideration; NGC 5813 is a galaxy group (Randall et al. 2011), while Cygnus A is at the center of a galaxy cluster (e.g., Steenbrugge et al. 2014). In this context, previous studies noted that the relative ratio of X-ray cavity heating power to cooling luminosity appears to be five times higher in low-mass systems than in rich clusters (e.g., Gitti et al. 2012). By separating the systems in our compilation between galaxy clusters (squares in Figure 8) and galaxy groups and elliptical galaxies (circles in Figure 8), we find that FR IIs have $P_{tot}/L_{cool} \geqslant 180$, while FR Is have $9 \leqslant P_{tot}/L_{cool} \leqslant 66$ in galaxy groups and elliptical galaxies. In galaxy clusters, FR IIs have $P_{tot}/L_{cool} \geqslant 50$, while FR Is have $0.5 \leqslant P_{tot}/L_{cool} \leqslant 16$. These values are consistent with AGNs in galaxy groups and elliptical galaxies having
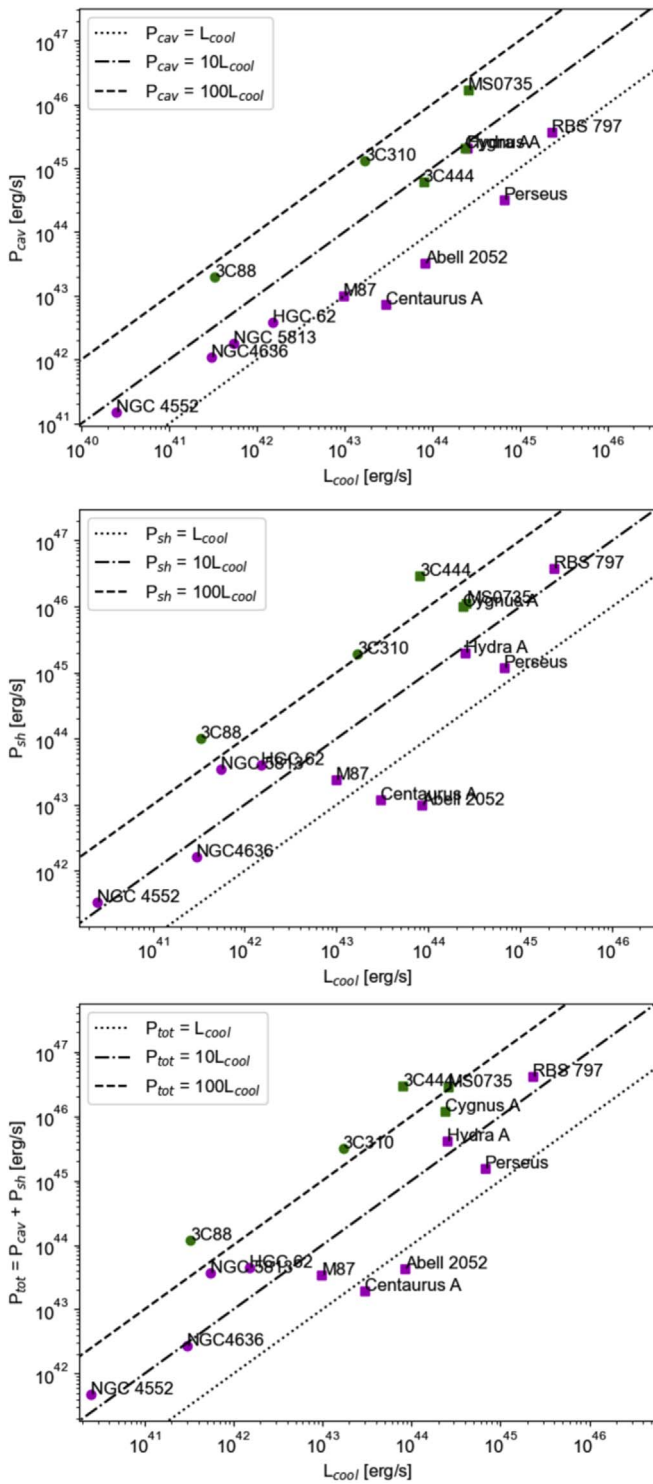
Figure 8. Mechanical cavity power (top panel), shock power (middle panel), and total heating power (bottom panel) vs. cooling luminosity for the 15 systems listed in Table 3. Overplotted are lines of $P/L_{cool} = 1$, 10, and 100. Dots are for elliptical galaxies and galaxy groups, while squares are for galaxy clusters. The color of the points indicates the FR type of the central radio galaxy; FR Is are in magenta, while FR IIs are in green.

achieve a self-regulated equilibrium between input fuel and output energy. However, FR IIs seem to be able to sustain more extreme feedback. In this respect, sources populating the upper space of the P_{tot}/L_{cool} plot may be expected to have more efficiently heated the ambient gas and quenched any residual cooling. We can test this scenario by considering that the entropy of the ICM is a good proxy for the cooling efficiency of the gas. Cavagnolo et al. (2009) analyzed the entropy profiles of 239 systems (the ACCEPT sample) and measured the central entropy K_0 that quantifies the typical excess of core entropy above the best-fitting power law found at larger radii. By cross-matching the list of Table 3 with the ACCEPT sample, we find that 11 out of 15 objects have tabulated values of K_0 (the missing sources are 3C 444, 3C 310, 3C 88, and NGC 4552). We additionally include 3C 88, since Liu et al. (2019) determined the core entropy of this group in a similar fashion to that of Cavagnolo et al. (2009). Based on the core entropy values for the systems in our list (see Table 3), we find that the hot atmospheres of FR I radio galaxies have K_0 in the range 1–20 keV cm^2 (with an average of 9 ± 8 keV cm^2, where the uncertainty is the dispersion around the mean). For the three FR IIs matching our criteria, the central entropy is in the range 7–24 keV cm^2 (with an average of 15 ± 8 keV cm^2). The clear overlap between the two classes indicates that differences of orders of magnitude in feedback output (i.e., the ratio between mechanical power and cooling luminosity) do not cause any overheating of the central gas. Therefore, we find that the FR IIs in the plots of Figure 8, while providing stronger feedback, are not dramatically quenching the cooling of the surrounding environment. This may suggest that the thermodynamic regulation of the ICM on long timescales (the central cooling time of these systems ranges between hundreds of megayears and ~1 Gyr) is resilient to episodic (the typical outburst ages are of a few tens of megayears), overpowered outburst episodes (for numerical simulations supporting this picture, see, e.g., Gaspari et al. 2011; Le Brun et al. 2014; Prasad et al. 2015; Duan & Guo 2020; Bourne & Sijacki 2021).

We note that these results are speculative and should be treated with caution. In particular, the values reported in Table 3 are subject to different assumptions made in the literature. For instance, cavity power depends on cavity age, which can be estimated with several methods. Moreover, the shock energy and power may be estimated as done in this work (and in, e.g., Randall et al. 2015; Liu et al. 2019) or by adopting a point explosion model tailored to the specific object (Nulsen et al. 2005). In any case, the difference between these varying assumptions is typically within a factor of a few (e.g., Bîrzan et al. 2004; Randall et al. 2011, 2015; Liu et al. 2019), while the trends we noticed in Figure 8 refer to differences of at least 1 order of magnitude. Thus, we argue that the effect of nonuniform assumptions is not dominant. On the other hand, the systems we considered are probably not representative of the population of galaxy clusters, galaxy groups, and elliptical galaxies. More likely, they represent the tip of the iceberg of an underlying larger population of objects with X-ray cavities and weak shocks launched by the central AGN that have not been detected due to limited statistics. As such, we do not provide correlations of P_{cav} versus L_{cool}, P_{sh} versus L_{cool}, or P_{tot} versus L_{cool}, limiting ourselves to discussing general trends. Enlarging the sample to allow a deeper, statistically consistent comparison is a future perspective of this work.

relatively more power to counter cooling than sources in galaxy clusters, with FR IIs always providing more violent feedback.

Overall, it appears that both classes of radio galaxies have mechanical power that correlates with the cooling luminosity of their hot atmospheres, suggesting that FR Is and FR IIs can

7. Conclusions

Our results can be summarized as follows.

1. We discovered that AGN activity in RBS 797 has driven three nested shock fronts, found at projected distances of 50, 80, and 130 kpc from the center, with Mach numbers in the range 1.2–1.3. We find that the total energy required to drive the shocks in RBS 797 is roughly 6×10^{61} erg. The mechanical power does not change drastically between the successive activity cycles, with the AGN driving a weak shock with power $P_{\rm sh} \approx 10^{46}$ erg s^{-1} every 20–30 Myr. Based on the morphology and timescales of the inner cocoon shock and E–W X-ray cavities (see also Ubertosi et al. 2021), we suggest that the bubbles and shock likely originate from the same outburst. Furthermore, we hypothesize that the amorphous shape of the radio source surrounding the X-ray cavities (at 50–100 kpc from the center) may be caused by the passage of the middle and outer shocks, which could have overrun and distorted preexisting radio plasma from previous AGN activity.

2. The inflation of X-ray cavities has left footprints in the ICM; we found hints of a ring of enhanced metallicity surrounding the bubbles between ∼30 and 50 kpc from the center, likely explained in the context of mechanical uplift of central enriched gas. The low-entropy ($\leqslant 30$ keV cm^2) and short cooling time ($t_{\rm cool} \leqslant 1$ Gyr) ICM is preferentially found between and behind the X-ray cavities, which may indicate that the bubbles are stimulating cooling. In this context, the region with the shortest cooling time (∼440 Myr) and minimum $t_{\rm cool}/t_{\rm ff}$ ratio (∼18) is located within 20 kpc S of the center, where filamentary patches of [O II] nebular emission tracing star-forming gas were recently detected (Calzadilla et al. 2022).

3. We estimated that within the cooling radius of RBS 797 ($r_{\rm cool}^{7.7\,{\rm Gyr}} = 109.3 \pm 1.0$ kpc), the X-ray emitting gas is radiating its energy at the remarkable rate of $L_{\rm cool} = (2.34 \pm 0.01) \times 10^{45}$ erg s^{-1}. Such radiative losses are overcome by the total mechanical power in RBS 797 (by shocks and X-ray cavities), i.e., 3.4×10^{46} erg s^{-1}. Moreover, the distance from the center to the outer shock (135 kpc) is larger than the cooling radius, suggesting that the gas outside $r = r_{\rm cool}$ is also being heated.

4. By evaluating shocks and cavity power ($P_{\rm sh}$ and $P_{\rm cav}$) versus cooling ($L_{\rm cool}$) for RBS 797 and 14 other well-known galaxy clusters, galaxy groups, and elliptical galaxies with detections of X-ray cavities and weak shocks, we find that the already-known scaling of $P_{\rm cav}$ versus $L_{\rm cool}$ also exists for $P_{\rm sh}$ versus $L_{\rm cool}$ and $P_{\rm tot}[=P_{\rm sh} + P_{\rm cav}]$ versus $L_{\rm cool}$. Additionally, while RBS 797 has the largest mechanical power and cooling luminosity, it is not the object with the most extreme feedback. In particular, we noted that systems with FR I radio galaxies at their center (as RBS 797) seem to have ratios $P_{\rm tot}/L_{\rm cool}$ within a few tens, while systems with central FR II AGNs have total mechanical power that can exceed the cooling luminosity of the surrounding atmosphere by more than 2 orders of magnitude. This difference becomes more evident when massive systems (clusters) are distinguished from smaller systems (groups and elliptical galaxies). Nevertheless, the central entropy of systems hosting FR Is is comparable to that of systems hosting FR IIs, suggesting that differences of orders of magnitude in feedback output do not overheat the central gas.

Facilities: CXO, JVLA.

Software: astropy (Astropy Collaboration et al. 2013, 2018), APLpy (Robitaille & Bressert 2012), Numpy (van der Walt et al. 2011; Harris et al. 2020), Scipy (Jones et al. 2001), CIAO (Fruscione et al. 2006), XSPEC (Arnaud 1996), AIPS (van Moorsel et al. 1996), CASA (McMullin et al. 2007).

Appendix A
Details of the Chandra X-Ray Observations of RBS 797

In Table A1, we list the Chandra ObsIDs analyzed in this paper (see Section 2.1).

Table A1
List of the Chandra Observations of RBS 797 Used in This Work

ObsID (1)	Instrument (2)	t_{raw} (ks) (3)	t_{clean} (ks) (4)	PI (5)
2202	ACIS-I	11.7	9.2	Schindler
7902	ACIS-S	38.3	37.3	McNamara
22636	ACIS-S	44.5	41.4	Gitti
22637	ACIS-S	23.7	22.1	Gitti
22638	ACIS-S	19.8	18.0	Gitti
22931	ACIS-S	24.7	23.4	Gitti
22932	ACIS-S	57.5	55.1	Gitti
22933	ACIS-S	24.7	22.8	Gitti
22934	ACIS-S	25.7	25.0	Gitti
22935	ACIS-S	25.7	23.9	Gitti
23332	ACIS-S	43.4	39.4	Gitti
24631	ACIS-S	24.7	23.3	Gitti
24632	ACIS-S	24.6	23.0	Gitti
24852	ACIS-S	43.5	39.1	Gitti
24865	ACIS-S	25.7	24.4	Gitti
Total		458.4	427.4	

Note. (1) Number of the observation, (2) Chandra instrument, (3) raw exposure time, (4) cleaned exposure time after removal of background flares, and (5) principal investigator. The last row shows the sum of the uncleaned and cleaned exposures.

Appendix B
Details of the Morphological and Spectral Analysis of Shock Fronts

In this section, we report the detailed results of the analysis of the shock fronts. We show in Table B1 the results of fitting surface brightness profiles encompassing each shock front with a broken power-law model and a power-law model. Furthermore, we summarize in Table B2 the geometry of the sectors we used as spectral extraction regions (columns (1)–(3)), the χ^2/d.o.f. (column (4)), and the best-fit parameters within the downstream and upstream sides of the shock. The values of temperature and pressure are deprojected. For each shock front, Figure B1 shows the region used to extract the spectrum of the upstream and downstream sides and the resulting temperature profile. Ultimately, we show in Figure B2 the comparison between using projct and DSDEPROJ (Sanders & Fabian 2007; Russell et al. 2008) to deproject the azimuthally averaged thermodynamic profiles described in Section 4.1. As it is possible to see, the two methods return consistent deprojected radial profiles. This confirms that the temperature jumps at the location of the shocks are not caused by the ringing effect associated with projct.

Table B1
Analysis of the Surface Brightness Profile of the Shocks in RBS 797

Shock (1)	Broken Power Law						Power Law				F-test	
	α_1 (2)	α_2 (3)	r_J (arcsec) (4)	S_0 (5)	J (6)	χ^2/d.o.f. (7)	α (8)	r_S (arcsec) (9)	S_0 (10)	χ^2/d.o.f. (11)	F (12)	p (13)
S1	-0.31 ± 0.08	1.35 ± 0.05	11.0 ± 0.1	4.1 ± 0.2	1.49 ± 0.07	13.2/7	2.14 ± 0.02	18.0 ± 1.0	0.14 ± 0.01	195.1/20	59.3	1.2×10^{-8}
S2	-0.23 ± 0.09	1.63 ± 0.07	10.3 ± 0.2	5.1 ± 0.6	1.40 ± 0.06	6.6/4	1.99 ± 0.02	16.8 ± 0.6	0.13 ± 0.01	176.7/19	51.6	6.0×10^{-8}
S_{in}	0.71 ± 0.05	1.36 ± 0.03	10.7 ± 0.1	3.3 ± 0.2	1.29 ± 0.03	14.4/8	1.67 ± 0.01	2.5 ± 0.1	4.8 ± 0.2	353.9/10	94.0	2.8×10^{-6}
S3	1.23 ± 0.03	1.49 ± 0.04	16.2 ± 0.1	0.77 ± 0.3	1.29 ± 0.04	25.6/18	2.14 ± 0.01	18.0 ± 1.0	0.14 ± 0.01	60.6/20	17.1	1.3×10^{-5}
S4	0.26 ± 0.09	1.64 ± 0.05	16.7 ± 0.2	0.94 ± 0.01	1.28 ± 0.05	10.1/10	2.10 ± 0.03	7.2 ± 0.1	0.69 ± 0.07	127.5/12	58.1	3.1×10^{-6}
S5	0.32 ± 0.10	1.95 ± 0.05	30.5 ± 0.4	0.23 ± 0.01	1.27 ± 0.04	6.1/6	2.63 ± 0.02	25.2 ± 0.3	0.16 ± 0.01	269.4/8	130	1.1×10^{-5}
S6	0.01 ± 0.09	1.39 ± 0.04	28.9 ± 0.2	0.69 ± 0.03	1.37 ± 0.04	24.3/15	2.05 ± 0.02	19.2 ± 0.6	0.38 ± 0.02	193.4/17	52.2	1.8×10^{-7}

Note. For each edge, we report the best-fit parameters using a broken power law (columns (2)–(7)) and a single power law (columns (8)–(11)). The last two columns show the result of an F-test between the two models. The reported r_J refers to the distance along the major axis of the ellipse used to describe each edge (see Table B2 for the geometric details). The normalizations S_0 are in units of 10^{-2} counts s^{-1} arcmin^{-2}. Corresponding surface brightness profiles are shown in Figure 2.

Table B2
Spectral Analysis of Three Pairs of Surface Brightness Edges

Shock	Ellipticity (P.A.)	$\theta_1 - \theta_2$	χ^2/d.o.f.	Side	R_i (kpc (arcsec))	R_o (kpc (arcsec))	kT (keV)	p_{ICM} (10^{-10} erg cm^{-3})
(1)	(2)	(3)	(4)	(5)	(6)	(7)	(8)	(9)
S1 (53.9 kpc)	1.2 (345°)	130°–190°	0.97	Downstream	45.6 (9.3)	53.9 (11)	$8.9^{+0.9}_{-0.8}$	$12.9^{+1.2}_{-1.1}$
				Upstream	53.9 (11)	63.7 (13)	$6.6^{+0.7}_{-0.7}$	$7.1^{+0.7}_{-0.7}$
S2 (50.5 kpc)	1.2 (345°)	310°–15°	1.08	Downstream	40.2 (8.2)	50.5 (10.3)	$5.4^{+0.4}_{-0.3}$	$9.8^{+1.0}_{-0.9}$
				Upstream	50.5 (10.3)	68.6 (14)	$4.8^{+0.2}_{-0.2}$	$6.5^{+0.6}_{-0.6}$
S$_{in}$ (52.4 kpc)	1.2 (345°)	0°–360°	0.98	Downstream	44.1 (9)	52.4 (10.7)	$5.9^{+0.4}_{-0.4}$	$10.1^{+0.7}_{-0.7}$
				Upstream	52.4 (10.3)	68.6 (14)	$5.0^{+0.2}_{-0.2}$	$5.4^{+0.3}_{-0.3}$
S3 (79.4 kpc)	1.1 (20°)	200°–270°	0.97	Downstream	63 (12.8)	79.4 (16.2)	$7.9^{+0.8}_{-0.8}$	$6.3^{+0.7}_{-0.7}$
				Upstream	79.4 (16.2)	108 (22)	$6.4^{+0.3}_{-0.4}$	$3.8^{+0.2}_{-0.3}$
S4 (81.8 kpc)	1.1 (20°)	45°–110°	0.91	Downstream	63.7 (13)	81.8 (16.7)	$6.7^{+0.6}_{-0.6}$	$6.3^{+0.6}_{-0.6}$
				Upstream	81.8 (16.7)	118 (24)	$5.4^{+0.4}_{-0.4}$	$2.7^{+0.2}_{-0.2}$
S5 (136 kpc)	1.1 (102°)	140°–252°	1.03	Downstream	113 (23)	149 (30.5)	$9.5^{+1.7}_{-1.6}$	$2.7^{+0.4}_{-0.4}$
				Upstream	149 (30.5)	226 (46.2)	$6.9^{+0.8}_{-0.8}$	$1.4^{+0.2}_{-0.1}$
S6 (132 kpc)	1.1 (102°)	304°–87°	0.99	Downstream	102 (21)	142 (28.9)	$8.3^{+1.7}_{-1.2}$	$2.9^{+0.8}_{-0.5}$
				Upstream	142 (28.9)	216 (44)	$5.9^{+0.7}_{-0.7}$	$1.3^{+0.2}_{-0.2}$

Note. (1) Name of the edge and distance from the center (measured from the front mid-aperture). (2) Ellipticity and P.A. of the sector used as the spectral extraction region. (3) Angular range intersecting the position of the edge. (4) χ^2/d.o.f. (5) Side of the edge (within: downstream; outside: upstream). (6)–(7) Inner and outer radii of the annular sector (along the major axis of the ellipse). (8) Deprojected ICM temperature. (9) Deprojected ICM pressure.
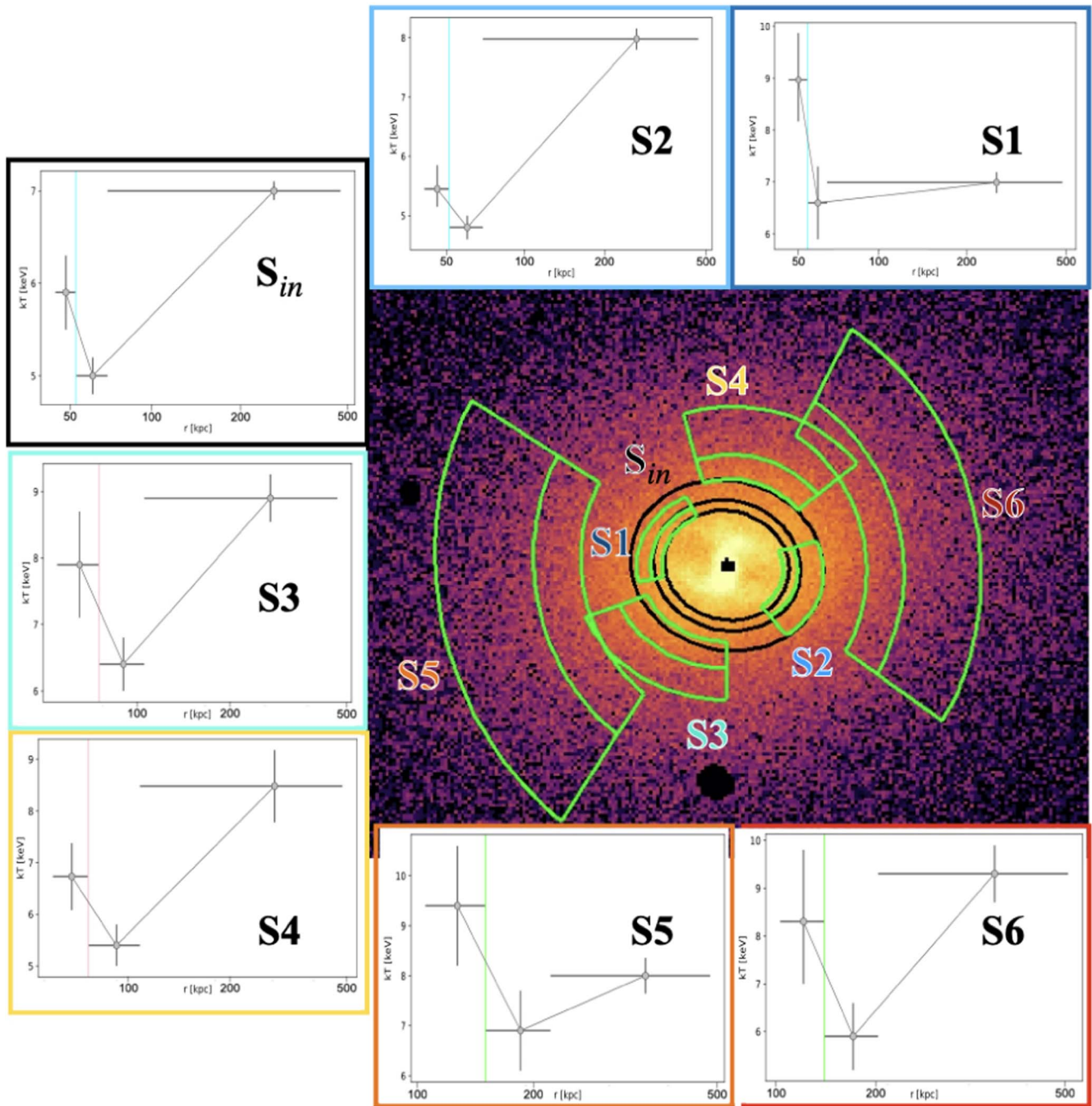
Figure B1. Central panel: 0.5–7 keV Chandra image of RBS 797. The green (black) sectors indicate the regions (described in Table B2) used to determine the thermodynamic properties across the downstream and upstream sides of the arc-like (cocoon-like) edges. A third region extending to the edge of the Chandra image has been used for deprojection (not shown in the figure). Colored labels indicate the name of each edge. Subpanels: deprojected temperature profile across each front. The vertical colored lines indicate the position of each shock.
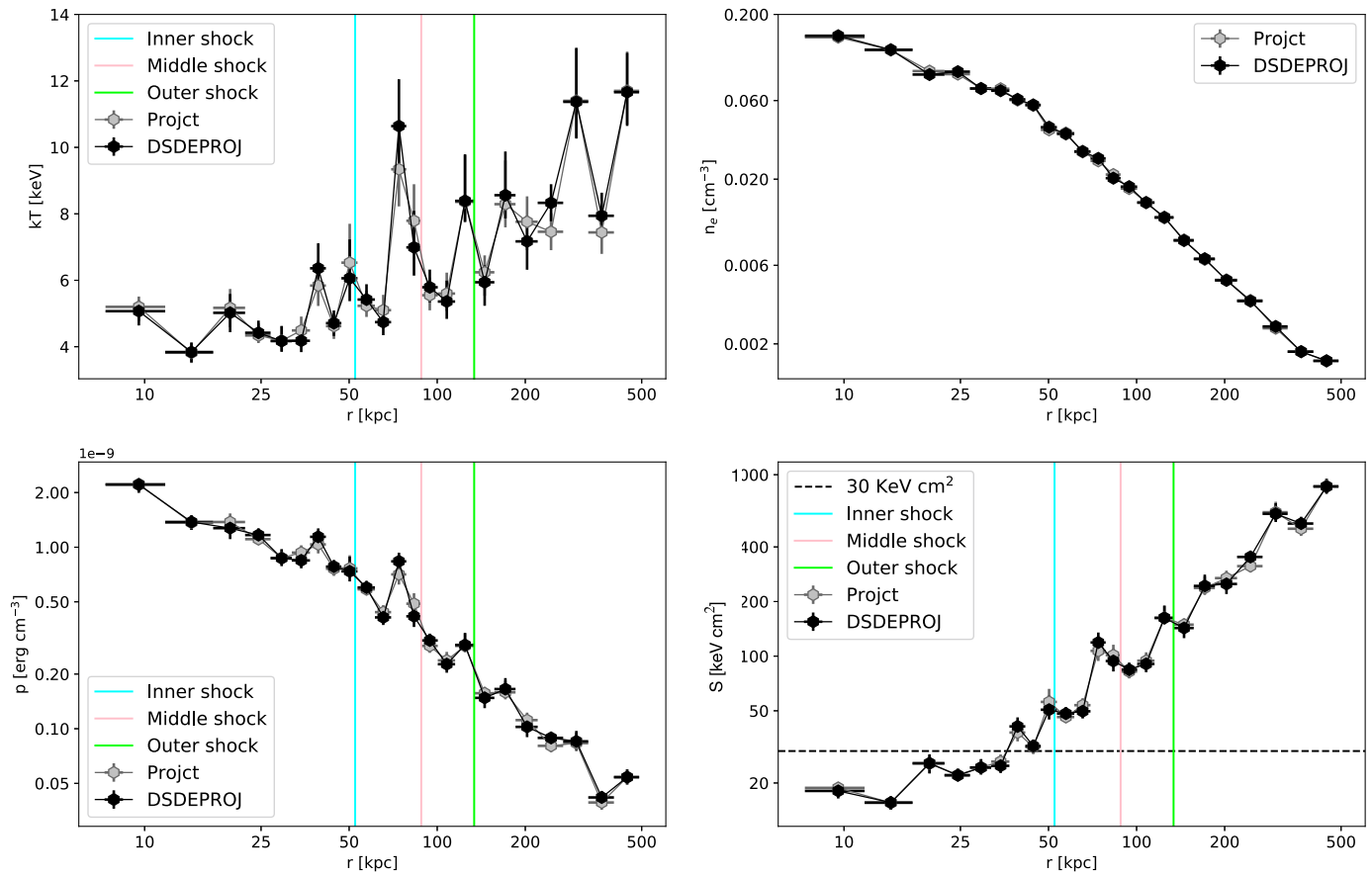
Figure B2. Comparison between the radial profiles of ICM thermodynamic quantities in RBS 797 using `projct` (gray points) and `DSDEPROJ` (black points). Upper left: deprojected temperature profiles. Upper right: electron density profile. Lower left: pressure profile. Lower right: entropy profile, with the horizontal dotted line showing the $S \leqslant 30$ keV cm^2 threshold for the condensation of the ICM into multiphase gas clouds. In the temperature, pressure, and entropy profiles, the colored vertical lines show the distance from the center of the three nested weak shocks.

ORCID iDs

F. Ubertosi ⓘ https://orcid.org/0000-0001-5338-4472
M. Gitti ⓘ https://orcid.org/0000-0002-0843-3009
F. Brighenti ⓘ https://orcid.org/0000-0001-9807-8479
M. McDonald ⓘ https://orcid.org/0000-0001-5226-8349
P. Nulsen ⓘ https://orcid.org/0000-0003-0297-4493
M. Donahue ⓘ https://orcid.org/0000-0002-2808-0853
G. Brunetti ⓘ https://orcid.org/0000-0003-4195-8613
S. Randall ⓘ https://orcid.org/0000-0002-3984-4337
M. Gaspari ⓘ https://orcid.org/0000-0003-2754-9258
S. Ettori ⓘ https://orcid.org/0000-0003-4117-8617
M. Calzadilla ⓘ https://orcid.org/0000-0002-2238-2105
A. Ignesti ⓘ https://orcid.org/0000-0003-1581-0092
L. Feretti ⓘ https://orcid.org/0000-0003-0312-6285
E. L. Blanton ⓘ https://orcid.org/0000-0002-0485-6573

References

Arnaud, K. A. 1996, in ASP Conf. Ser. 101, Astronomical Data Analysis Software and Systems V, ed. G. H. Jacoby & J. Barnes (San Francisco, CA: ASP), 17
Asplund, M., Grevesse, N., Sauval, A. J., & Scott, P. 2009, ARA&A, 47, 481
Astropy Collaboration, Price-Whelan, A. M., Sipőcz, B. M., et al. 2018, AJ, 156, 123
Astropy Collaboration, Robitaille, T. P., Tollerud, E. J., et al. 2013, A&A, 558, A33
Babul, A., Sharma, P., & Reynolds, C. S. 2013, ApJ, 768, 11
Baldi, A., Forman, W., Jones, C., et al. 2009, ApJ, 707, 1034
Biava, N., Brienza, M., Bonafede, A., et al. 2021, A&A, 650, A170
Bîrzan, L., McNamara, B. R., Nulsen, P. E. J., Carilli, C. L., & Wise, M. W. 2008, ApJ, 686, 859
Bîrzan, L., Rafferty, D. A., Brüggen, M., & Intema, H. T. 2017, MNRAS, 471, 1766
Bîrzan, L., Rafferty, D. A., McNamara, B. R., Nulsen, P. E. J., & Wise, M. W. 2009, in AIP Conf. Proc. 1201, The Monster's Fiery Breath: Feedback in Galaxies, Groups, and Clusters, ed. S. Heinz & E. Wilcots (Melville, NY: AIP), 301
Bîrzan, L., Rafferty, D. A., McNamara, B. R., Wise, M. W., & Nulsen, P. E. J. 2004, ApJ, 607, 800
Bîrzan, L., Rafferty, D. A., Nulsen, P. E. J., et al. 2012, MNRAS, 427, 3468
Blanton, E. L., Randall, S. W., Clarke, T. E., et al. 2011, ApJ, 737, 99
Blanton, E. L., Randall, S. W., Douglass, E. M., et al. 2009, ApJL, 697, L95
Boehringer, H., Voges, W., Fabian, A. C., Edge, A. C., & Neumann, D. M. 1993, MNRAS, 264, L25
Bogdán, Á., van Weeren, R. J., Kraft, R. P., et al. 2014, ApJL, 782, L19
Bourne, M. A., & Sijacki, D. 2021, MNRAS, 506, 488
Brighenti, F., & Mathews, W. G. 2002, ApJ, 573, 542
Brighenti, F., & Mathews, W. G. 2006, ApJ, 643, 120
Brighenti, F., Mathews, W. G., & Temi, P. 2015, ApJ, 802, 118
Brüggen, M., Heinz, S., Roediger, E., Ruszkowski, M., & Simionescu, A. 2007, MNRAS Lett., 380, L67
Brunetti, G., & Jones, T. W. 2014, IJMPD, 23, 1430007
Buote, D. A. 1999, MNRAS, 309, 685
Calzadilla, M. S., McDonald, M., Donahue, M., et al. 2022, ApJ, 940, 140
Cavagnolo, K. W., Donahue, M., Voit, G. M., & Sun, M. 2009, ApJS, 182, 12
Cavagnolo, K. W., McNamara, B. R., Nulsen, P. E. J., et al. 2010, ApJ, 720, 1066
Cavagnolo, K. W., McNamara, B. R., Wise, M. W., et al. 2011, ApJ, 732, 71
Churazov, E., Brüggen, M., Kaiser, C. R., Böhringer, H., & Forman, W. 2001, ApJ, 554, 261
Churazov, E., Forman, W., Jones, C., & Böhringer, H. 2000, A&A, 356, 788
Cielo, S., Babul, A., Antonuccio-Delogu, V., Silk, J., & Volonteri, M. 2018, A&A, 617, A58
Croston, J. H., Hardcastle, M. J., Mingo, B., et al. 2011, ApJL, 734, L28
Croston, J. H., Kraft, R. P., Hardcastle, M. J., et al. 2009, MNRAS, 395, 1999
David, L. P., Nulsen, P. E. J., McNamara, B. R., et al. 2001, ApJ, 557, 546
Donahue, M., & Voit, G. M. 2004, in Clusters of Galaxies: Probes of Cosmological Structure and Galaxy Evolution, ed. J. S. Mulchaey, A. Dressler, & A. Oemler (Cambridge: Cambridge Univ. Press), 143
Donahue, M., & Voit, G. M. 2022, PhR, 973, 1
Doria, A., Gitti, M., Ettori, S., et al. 2012, ApJ, 753, 47
Duan, X., & Guo, F. 2020, ApJ, 896, 114

Dunn, R. J. H., Fabian, A. C., & Taylor, G. B. 2005, MNRAS, 364, 1343
Eckert, D., Gaspari, M., Gastaldello, F., Le Brun, A. M. C., & O'Sullivan, E. 2021, Univ, 7, 142
Fabian, A. C. 2012, ARA&A, 50, 455
Fabian, A. C., Nulsen, P. E. J., & Canizares, C. R. 1984, Natur, 310, 733
Fabian, A. C., Reynolds, C. S., Taylor, G. B., & Dunn, R. J. H. 2005, MNRAS, 363, 891
Fabian, A. C., Sanders, J. S., Taylor, G. B., et al. 2006, MNRAS, 366, 417
Fanaroff, B. L., & Riley, J. M. 1974, MNRAS, 167, 31P
Forman, W., Churazov, E., Jones, C., et al. 2017, ApJ, 844, 122
Forman, W., Jones, C., Churazov, E., et al. 2007, ApJ, 665, 1057
Forman, W., Nulsen, P., Heinz, S., et al. 2005, ApJ, 635, 894
Fruscione, A., McDowell, J. C., Allen, G. E., et al. 2006, Proc. SPIE, 6270, 62701V
Fujita, Y., Kawakatu, N., & Shlosman, I. 2016, PASJ, 68, 26
Gaspari, M., Brighenti, F., & Temi, P. 2012, MNRAS, 424, 190
Gaspari, M., Melioli, C., Brighenti, F., & D'Ercole, A. 2011, MNRAS, 411, 349
Gaspari, M., Tombesi, F., & Cappi, M. 2020, NatAs, 4, 10
Gastaldello, F., Ettori, S., Balestra, I., et al. 2010, in The Energetic Cosmos: From Suzaku to ASTRO-H, Proc. 3rd Suzaku Conf., ed. K. Makishima (Otaru, Japan: JAXA), 94
Giodini, S., Smolčić, V., Finoguenov, A., et al. 2010, ApJ, 714, 218
Gitti, M., Brighenti, F., & McNamara, B. R. 2012, AdAst, 2012, 950641
Gitti, M., Feretti, L., & Schindler, S. 2006, A&A, 448, 853
Gitti, M., Giroletti, M., Giovannini, G., Feretti, L., & Liuzzo, E. 2013, A&A, 557, L14
Gitti, M., McNamara, B. R., Nulsen, P. E. J., & Wise, M. W. 2007, ApJ, 660, 1118
Gitti, M., Nulsen, P. E. J., David, L. P., McNamara, B. R., & Wise, M. W. 2011, ApJ, 732, 13
Gitti, M., O'Sullivan, E., Giacintucci, S., et al. 2010, ApJ, 714, 758
Graham, J., Fabian, A. C., & Sanders, J. S. 2008a, MNRAS, 391, 1749
Graham, J., Fabian, A. C., & Sanders, J. S. 2008b, MNRAS, 386, 278
Gültekin, K., King, A. L., Cackett, E. M., et al. 2019, ApJ, 871, 80
Harris, C. R., Millman, K. J., van der Walt, S. J., et al. 2020, Natur, 585, 357
Heinz, S., & Churazov, E. 2005, ApJL, 634, L141
HI4PI Collaboration, Ben Bekhti, N., Flöer, L., et al. 2016, A&A, 594, A116
Hlavacek-Larrondo, J., Fabian, A. C., Edge, A. C., et al. 2012, MNRAS, 421, 1360
Hlavacek-Larrondo, J., McDonald, M., Benson, B. A., et al. 2015, ApJ, 805, 35
Hudson, D. S., Mittal, R., Reiprich, T. H., et al. 2010, A&A, 513, A37
Huško, F., Lacey, C. G., Schaye, J., Schaller, M., & Nobels, F. S. J. 2022, MNRAS, 516, 3750
Jones, C., Forman, W., Vikhlinin, A., et al. 2002, ApJL, 567, L115
Jones, E., Oliphant, T., Peterson, P., et al. 2001, SciPy: Open source scientific tools for Python, https://www. scipy. org
Kirkpatrick, C. C., & McNamara, B. R. 2015, MNRAS, 452, 4361
Kirkpatrick, C. C., McNamara, B. R., & Cavagnolo, K. W. 2011, ApJL, 731, L23
Kraft, R. P., Birkinshaw, M., Nulsen, P. E. J., et al. 2012, ApJ, 749, 19
Le Brun, A. M. C., McCarthy, I. G., Schaye, J., & Ponman, T. J. 2014, MNRAS, 441, 1270
Liu, W., Sun, M., Nulsen, P., et al. 2019, MNRAS, 484, 3376
Liu, W., Sun, M., Nulsen, P. E. J., et al. 2020, MNRAS, 492, 3156
Machacek, M., Nulsen, P. E. J., Jones, C., & Forman, W. R. 2006, ApJ, 648, 947
Markevitch, M., & Vikhlinin, A. 2007, PhR, 443, 1
Martizzi, D., Quataert, E., Faucher-Giguère, C.-A., & Fielding, D. 2019, MNRAS, 483, 2465
Mathews, W. G., & Brighenti, F. 2003, ARA&A, 41, 191
Mathews, W. G., Faltenbacher, A., & Brighenti, F. 2006, ApJ, 638, 659
McCarthy, I. G., Schaye, J., Ponman, T. J., et al. 2010, MNRAS, 406, 822
McDonald, M., Gaspari, M., McNamara, B. R., & Tremblay, G. R. 2018, ApJ, 858, 45
McDonald, M., Veilleux, S., Rupke, D. S. N., & Mushotzky, R. 2010, ApJ, 721, 1262
McMullin, J. P., Waters, B., Schiebel, D., Young, W., & Golap, K. 2007, in ASP Conf. Ser. 376, Astronomical Data Analysis Software and Systems XVI, ed. R. A. Shaw, F. Hill, & D. J. Bell (San Francisco, CA: ASP), 127
McNamara, B. R., & Nulsen, P. E. J. 2007, ARA&A, 45, 117
McNamara, B. R., & Nulsen, P. E. J. 2012, NJPh, 14, 055023
McNamara, B. R., Nulsen, P. E. J., Wise, M. W., et al. 2005, Natur, 433, 45
McNamara, B. R., Russell, H. R., Nulsen, P. E. J., et al. 2016, ApJ, 830, 79
Nulsen, P. E. J., McNamara, B. R., Wise, M. W., & David, L. P. 2005, ApJ, 628, 629
Olivares, V., Salome, P., Hamer, S. L., et al. 2022, A&A, 666, A94

O'Sullivan, E., Giacintucci, S., David, L. P., et al. 2011, ApJ, 735, 11
O'Sullivan, E., Vrtilek, J. M., & Kempner, J. C. 2005, ApJL, 624, L77
Peterson, J. R., & Fabian, A. C. 2006, PhR, 427, 1
Prasad, D., Sharma, P., & Babul, A. 2015, ApJ, 811, 108
Rafferty, D. A., McNamara, B. R., Nulsen, P. E. J., & Wise, M. W. 2006, ApJ, 652, 216
Randall, S. W., Forman, W. R., Giacintucci, S., et al. 2011, ApJ, 726, 86
Randall, S. W., Nulsen, P. E. J., Jones, C., et al. 2015, ApJ, 805, 112
Revaz, Y., Combes, F., & Salomé, P. 2008, A&A, 477, L33
Robitaille, T., & Bressert, E. 2012, APLpy: Astronomical Plotting Library in Python, Astrophysics Source Code Library, ascl:1208.017
Rossetti, M., Ghizzardi, S., Molendi, S., & Finoguenov, A. 2007, A&A, 463, 839
Russell, H. R., McNamara, B. R., Fabian, A. C., et al. 2019, MNRAS, 490, 3025
Russell, H. R., Sanders, J. S., & Fabian, A. C. 2008, MNRAS, 390, 1207
Sanders, J. S. 2006, MNRAS, 371, 829
Sanders, J. S., & Fabian, A. C. 2007, MNRAS, 381, 1381
Sanders, J. S., Fabian, A. C., Russell, H. R., Walker, S. A., & Blundell, K. M. 2016, MNRAS, 460, 1898
Schindler, S., Castillo-Morales, A., De Filippis, E., Schwope, A., & Wambsganss, J. 2001, A&A, 376, L27
Schmidt, R. W., Fabian, A. C., & Sanders, J. S. 2002, MNRAS, 337, 71
Shin, J., Woo, J.-H., & Mulchaey, J. S. 2016, ApJS, 227, 31
Snios, B., Nulsen, P. E. J., Wise, M. W., et al. 2018, ApJ, 855, 71
Soker, N. 2022, Univ, 8, 483
Steenbrugge, K. C., Blundell, K. M., & Pyrzas, S. 2014, A&A, 563, A131
Sutherland, R. S., & Dopita, M. A. 1993, ApJS, 88, 253
Temi, P., Gaspari, M., Brighenti, F., et al. 2022, ApJ, 928, 150
Ubertosi, F., Gitti, M., Brighenti, F., et al. 2021, ApJL, 923, L25
Vagshette, N. D., Naik, S., Patil, M., & Sonkamble, S. S. 2017, MNRAS, 466, 2054
Vagshette, N. D., Naik, S., & Patil, M. K. 2019, MNRAS, 485, 1981
van der Walt, S., Colbert, S. C., & Varoquaux, G. 2011, CSE, 13, 22
van Moorsel, G., Kemball, A., & Greisen, E. 1996, in ASP Conf. Ser. 101, Astronomical Data Analysis Software and Systems V, ed. G. H. Jacoby & J. Barnes (San Francisco, CA: ASP), 37
Vantyghem, A. N., McNamara, B. R., Russell, H. R., et al. 2014, MNRAS, 442, 3192
Voigt, L. M., & Fabian, A. C. 2006, MNRAS, 368, 518
Voit, G. M., & Donahue, M. 2015, ApJL, 799, L1
Wise, M. W., McNamara, B. R., Nulsen, P. E. J., Houck, J. C., & David, L. P. 2007, ApJ, 659, 1153
Wittor, D., & Gaspari, M. 2020, MNRAS, 498, 4983